PFC/JA-84-11

COMPTON AND RAMAN FREE ELECTRON LASER STABILITY PROPERTIES FOR A COLD ELECTRON BEAM PROPAGATING THROUGH A HELICAL MAGNETIC WIGGLER

John A. Davies
Ronald C. Davidson
George L. Johnston

Plasma Fusion Center
Massachusetts Institute of Technology
Cambridge, Massachusetts 02139

May, 1984

COMPTON AND RAMAN FREE ELECTRON LASER STABILITY PROPERTIES FOR A COLD ELECTRON BEAM PROPAGATING THROUGH A HELICAL MAGNETIC WIGGLER

John A. Davies
Clark University
Worcester, Massachusetts 01610

Ronald C. Davidson[†]
Science Applications, Inc.
Boulder, Colorado 80302

George L. Johnston
Plasma Fusion Center
Massachusetts Institute of Technology
Cambridge, Massachusetts 02139

ABSTRACT

This paper gives an extensive characterization of the range of validity of the Compton and Raman approximations to the exact free electron laser dispersion relation for a cold, relativistic electron beam propagating through a constant-amplitude helical wiggler magnetic field $\underset{\sim}{B}_w=-B_0\cos k_0 z\hat{\underset{\sim}{e}}_x-B_0\sin k_0 z\hat{\underset{\sim}{e}}_y$. Here $\lambda_0=2\pi/k_0$ is the wiggler wavelength, B_0 the wiggler amplitude (assumed constant), and the electron beam is treated as infinite in transverse extent. For example, a detailed numerical analysis shows that the Compton approximation ($\delta\phi\simeq 0$) gives a valid estimate, to within ten percent, of the maximum growth rate of the upshifted emission peak for system parameters satisfying

$$\frac{\omega_p c k_0}{\omega_c^2} < \frac{\gamma_b^3}{25}\,\frac{(1+\beta_b)}{\beta_b} .$$

Here, $\omega_p^2=4\pi n_0 e^2/\gamma_0 m$ is the relativistic plasma frequency-squared, $\omega_c=eB_0/\gamma_0 mc$ is the relativistic cyclotron frequency, $\gamma_b=(1-\beta_b^2)^{-1/2}$ is the relativistic mass factor, $\beta_b c=p_0/\gamma_0 m$ is the axial beam velocity, γ_0 is defined by $\gamma_0\equiv(1+p_0^2/m^2c^2+e^2B_0^2/m^2c^4k_0^2)^{1/2}$, and $G_0(p_z)=\delta(p_z-p_0)$ is the equilibrium axial momentum distribution of the beam electrons.

[†] Permanent address: Massachusetts Institute of Technology, Cambridge, MA, 02139.

I. INTRODUCTION

Recently Davidson and Uhm[1] have developed a fully self-consistent treatment of the free electron laser instability based on the Vlasov-Maxwell equations. Their analysis treats an intense relativistic electron beam, with uniform cross section, propagating through a constant amplitude magnetic field approximating a helical wiggler field [Eq. (1)]. The description includes beam kinetic effects and coupling to higher harmonics of the wiggler wavenumber k_0, and makes no a priori assumptions that any off-diagonal elements of the dispersion matrix [Eq. (9)] are negligibly small. The class of distribution functions considered in Ref. 1 is a product of delta functions of the transverse canonical momenta, including electromagnetic components, times a function $G(z,p_z,t)$ of axial position, momentum and time [Eq. (2)]. The complete dispersion relation [Eq. (20)] obtained in this analysis[1] is referred to as the full dispersion relation (FDR).

We are engaged in analytic and numerical studies of the properties of the FDR [Eq. (20)] and the corresponding matrix dispersion equation [Eq. (9)]. The work has proceeded at three levels: a study of the cold-fluid (cold-beam) FDR, of the warm-fluid FDR, and of the complete Vlasov-Maxwell FDR. There are two general goals of this work. The first goal is to identify important qualitative properties of the solutions of the FDR. Because of the few approximations made in the derivation of this dispersion relation, these properties can be expected to be reflected in the physics of the free electron laser instability and are not simply characteristic of the model. The second goal is to compare solutions of the FDR with those of approximate dispersion relations. Such comparisons enable one to determine the range of validity of such approximations, and more importantly, to identify the key physical processes contributing to the instability.

In this paper, we restrict the detailed stability analysis to the cold-beam version of the FDR [Eq. (28)]. The cold-beam stability properties discussed below, many of which are new, provide a point of reference for the inclusion of thermal effects which will be considered in subsequent papers. Most of the techniques applied here for a cold electron beam, can be extended directly to the case where the electrons are treated as a warm fluid. However, in the latter case, the introduction and application of these techniques are not so simple and straightforward as in the cold-beam case.

Section II begins with a concise outline of the principal analytic results of the Vlasov-Maxwell treatment in Ref. 1, including the matrix dispersion equation [Eq. (9)] and the full dispersion relation (FDR) in Eq. (20). Analytic expressions are obtained for the ratios of the electromagnetic energies (averaged over one cycle) contained in the left- and right-hand circularly-polarized radiation fields and in the longitudinal fields [Eqs. (24) - (26)]. An important result in this section is the full Compton dispersion relation (CDR) given in Eq. (27). Its derivation is the same as that of the FDR in Eq. (20), with the additional assumption that the longitudinal field is negligibly small ($\delta\phi \simeq 0$). The cold-beam limits of the FDR and CDR are then obtained [Eqs. (28) and (33)], as are the corresponding limits of the field energy ratios [Eqs. (35) - (37)]. These cold-beam results are then used in the remainder of the paper.

Detailed properties of the cold-beam FDR and CDR growth curves [$\mathrm{Im}(\hat{\omega})$ versus $\hat{k}$] are rigorously derived in Secs. III and V. As one result of this analysis, we conclude that the growth rate curves obtained from the cold-beam CDR [Eq. (33)] are not generally valid, except possibly in the vicinity of the maximum growth regions (as functions of $\hat{k}$) obtained from the FDR in Eq. (28) (Sec. VI). A criterion is established for classifying cold-beam systems as Compton or Raman based upon the accuracy of the growth rate obtained from the CDR at the upshifted maximum of the growth rate curve obtained from the FDR. (In this paper, the Raman classification is applied to any system for which the CDR is not a valid approximation at the maximum growth of the upshifted peak.) Using a combination of analytic and numerical studies, we obtain a condition for the validity of the Compton approximation for a cold electron beam. The validity condition for the Compton approximation is given by [Eq. (64)]

$$\frac{\omega_p c k_0}{\omega_c^2} < \frac{\gamma_b^3}{25} \frac{(1+\beta_b)}{\beta_b} ,$$

where ω_p, ω_c, γ_b, and β_b are defined in Eqs. (18), (19), (30), and (31), respectively.

An immediate result of the analysis in Secs. III and IV is the derivation of a sufficient condition for stability of a cold-beam system, i.e., $\mathrm{Im}(\hat{\omega})=0$ for all $\hat{k}$. This condition is given in Eq. (53). A numerical example showing the approach to stability with increasing beam density is presented in Fig. 6.

In Sec. VII, we obtain an approximate dispersion relation [Eq. (68)] known as the Raman approximation (RA) to the FDR. This dispersion relation [Eq. (68)] is applicable when the primary coupling is between the left-hand polarized radiation field and the negative-energy longitudinal field.

Detailed numerical examples comparing stability results from the FDR, CDR, and RA dispersion relations are presented in Sec. VIII.

These confirm several analytic results obtained in previous sections. Plots of frequency mismatches as functions of $\hat{k}$ over the (upshifted) growth regions are also presented, since assumptions regarding the relative values of these mismatches form the basis for most approximate dispersion relations applied to the free electron laser instability. The numerical analysis in Sec. VIII shows that the relative values of the frequency mismatches may vary significantly over the growth interval. Thus, approximations to the FDR which are valid at maximum growth do not necessarily give a valid description of the detailed shape of the growth curve, $\mathrm{Im}(\hat{\omega})$ versus $\hat{k}$.

The numerical analysis shows that an important feature of the FDR growth curves for cold-beam Compton systems is a tail extending from the maximum growth in the direction of increasing $\hat{k}$. In Sec. IX, it is shown that the instability in the tail region is produced by a coupling of the positive- and negative-energy longitudinal oscillations with the wiggler and radiation fields. We derive a condition for the existence of this tail, applicable to high-gamma systems with $2\gamma_b^2 \gg 1 + \omega_p^2/c^2k_0^2$.

II. DISPERSION RELATION

A. Introduction and Background

In Ref. 1, Davidson and Uhm developed a self-consistent description of the free electron laser instability for a relativistic electron beam propagating in the z-direction through a left-circularly-polarized helical wiggler field of the form

$$\underset{\sim}{B}_w = -B_0 \cos k_0 z \hat{\underset{\sim}{e}}_x - B_0 \sin k_0 z \hat{\underset{\sim}{e}}_y \ , \qquad (1)$$

where B_0 = const. is the wiggler amplitude and $\lambda_0 = 2\pi/k_0$ is the wiggler wavelength. In the linear stability analysis, it is assumed that the equilibrium self-electric and self-magnetic fields are negligibly small, that perturbations depend only upon axial coordinate z, and that the beam is cold in the transverse directions. It is further assumed that the beam distribution function $f_b(z,p,t)$ is of the form

$$f_b(z,p,t) = n_0 \delta(P_x) \delta(P_y) G(z,p_z,t) \ , \qquad (2)$$

where P_x and P_y are the canonical momenta[1] transverse to the beam propagation direction, and p_z is the mechanical momentum in the z-direction. The distribution function $G(z,p_z,t)$ satisfies the one-dimensional nonlinear Vlasov equation[1]

$$\left(\frac{\partial}{\partial t} + v_z \frac{\partial}{\partial z} - \frac{\partial}{\partial z} \hat{H}(z,p_z,t) \frac{\partial}{\partial p_z} \right) G(z,p_z,t) = 0 \ . \qquad (3)$$

The quantity $\hat{H}(z,p_z,t) = [m^2c^4 + c^2p_z^2 + e^2(A_x^0 + \delta A_x)^2 + e^2(A_y^0 + \delta A_y)^2]^{1/2} - e\delta\phi(z,t)$ is the potential giving rise to axial forces on an electron due to ponderomotive and longitudinal electrostatic forces.[1] The equilibrium one-dimensional distribution function is denoted by $G_0(p_z)$. In the equilibrium configuration, the energy

$$\gamma mc^2 = [m^2c^4+p_z^2c^2+B_0^2e^2/k_0^2]^{1/2} , \tag{4}$$

is conserved, as is the axial momentum

$$p_z = \gamma mv_z . \tag{5}$$

In the subsequent analysis, we consider the following three perturbed field quantities: (a) the vector potential for the left-circularly-polarized radiation field with wavenumber $k-k_0$ and frequency ω,

$$\delta A^-_{k-k_0} = \frac{A^-_{k-k_0}}{\sqrt{2}} \exp[i(k-k_0)z-i\omega t] , \tag{6}$$

(b) the vector potential for the right-circularly-polarized radiation field with wavenumber $k+k_0$ and frequency ω,

$$\delta A^+_{k+k_0} = \frac{A^+_{k+k_0}}{\sqrt{2}} \exp[i(k+k_0)z-i\omega t] , \tag{7}$$

and (c) the scalar potential for the longitudinal electric field with wavenumber k,

$$\delta\phi_k = \phi_k \exp(ikz-i\omega t) . \tag{8}$$

In Ref. 1, use is made of the linearized Vlasov-Maxwell equations to show that the perturbation amplitudes are related by the matrix dispersion equation

$$\begin{bmatrix} \hat{D}^T_{k+k_0} + \frac{1}{2}\hat{\omega}_c^2(\alpha_3\hat{\omega}_p^2+\hat{\chi}_k^{(2)}) , & \frac{1}{2}\hat{\omega}_c^2(\alpha_3\hat{\omega}_p^2+\hat{\chi}_k^{(2)}) , & -\hat{\omega}_c\hat{\chi}_k^{(1)} \\ \frac{1}{2}\hat{\omega}_c^2(\alpha_3\hat{\omega}_p^2+\hat{\chi}_k^{(2)}) , & \hat{D}^T_{k-k_0} + \frac{1}{2}\hat{\omega}_c^2(\alpha_3\hat{\omega}_p^2+\hat{\chi}_k^{(2)}) , & -\hat{\omega}_c\hat{\chi}_k^{(1)} \\ -\hat{\omega}_c\hat{\chi}_k^{(1)} , & -\hat{\omega}_c\hat{\chi}_k^{(1)} & 2\hat{D}^L_k \end{bmatrix} \begin{bmatrix} A^+_{k+k_0} \\ A^-_{k-k_0} \\ \phi_k \end{bmatrix} = 0 . \tag{9}$$

Higher-order couplings are included in the derivation of Eq. (9). Definitions of the quantities appearing in the above matrix dispersion equation are the following. The (dimensionless) longitudinal dielectric function and the transverse dielectric functions are given by[1]

$$\hat{D}^L_k = \hat{k}^2 + \hat{\chi}_k^{(0)}(\hat{\omega}) , \tag{10}$$

$$\hat{D}^T_{k-k_0} = \hat{\omega}^2 - (\hat{k}-1)^2 - \alpha_1\hat{\omega}_p^2 , \tag{11}$$

and

$$\hat{D}^T_{k+k_0} = \hat{\omega}^2 - (\hat{k}+1)^2 - \alpha_1\hat{\omega}_p^2 . \tag{12}$$

The dimensionless susceptibilities are defined by

$$\hat{\chi}_k^{(0)} = \bar{\gamma}mc\hat{\omega}_p^2 \int dp_z \frac{\hat{k}\partial G_0/\partial p_z}{\hat{\omega}-\hat{k}v_z/c} , \tag{13}$$

$$\hat{\chi}_k^{(1)} = \bar{\gamma}mc\hat{\omega}_p^2\bar{\gamma} \int \frac{dp_z}{\gamma} \frac{\hat{k}\partial G_0/\partial p_z}{\hat{\omega}-\hat{k}v_z/c} , \tag{14}$$

and

$$\hat{\chi}_k^{(2)} = \bar{\gamma}mc\hat{\omega}_p^2\bar{\gamma}^2 \int \frac{dp_z}{\gamma^2} \frac{\hat{k}\partial G_0/\partial p_z}{\hat{\omega}-\hat{k}v_z/c} , \tag{15}$$

where $\bar{\gamma}mc^2$ = const. is the characteristic electron energy and α_1 and α_3 are defined by

$$\alpha_n = \bar{\gamma}^n \int \frac{dp_z}{\gamma^n} G_0(p_z) \ . \tag{16}$$

The remaining dimensionless quantities are defined by

$$\hat{k} = k/k_0 \ , \tag{17}$$

$$\hat{\omega}_c = \frac{\omega_c}{ck_0} \ , \text{ where } \omega_c = \frac{eB_0}{\bar{\gamma}mc} \ , \tag{18}$$

and

$$\hat{\omega}_p^2 = \frac{\omega_p^2}{c^2k_0^2} \ , \text{ where } \omega_p^2 = \frac{4\pi n_0 e^2}{\bar{\gamma}m} \ . \tag{19}$$

We refer to the secular equation corresponding to the matrix dispersion equation (9) as the full dispersion relation (FDR). The FDR is given by[1]

$$\begin{aligned}
&\hat{D}_k^L(\hat{\omega})\hat{D}_{k+k_0}^T(\hat{\omega})\hat{D}_{k-k_0}^T(\hat{\omega}) \\
&\quad = \frac{1}{2}\,\hat{\omega}_c^2[\hat{D}_{k+k_0}^T(\hat{\omega})+\hat{D}_{k-k_0}^T(\hat{\omega})]\left\{[\hat{\chi}_k^{(1)}(\hat{\omega})]^2-\hat{D}_k^L(\hat{\omega})[\alpha_3\hat{\omega}_p^2+\hat{\chi}_k^{(2)}(\hat{\omega})]\right\}=0.
\end{aligned} \tag{20}$$

No assumption that any of the dielectric functions, the wiggler field, or the beam density is small has been made in deriving Eq. (20).

We return briefly to the effective potential $\hat{H}(z,p_z,t)$ appearing in Eq. (3). In Ref. 1, it is shown (after linearization) that the portion of $\hat{H}(z,p_z,t)$ contributing to the ponderomotive and longitudinal electrostatic forces on an electron is proportional to

$$\frac{1}{2}\,\hat{\omega}_c\,\frac{\bar{\gamma}}{\gamma}\left[\exp(ik_0z)\delta A_- + \exp(-ik_0z)\delta A_+\right] - \delta\phi \ , \tag{21}$$

where $\delta A_\pm = \delta A_x \pm i\delta A_y$ is the vector potential for the left- and right-circularly-polarized radiation fields and $\delta\phi$ is the longitudinal potential. It follows that the harmonics of the pondermotive and longitudinal potentials with normalized wavenumber $\hat{k}$ and frequency $\hat{\omega}$ have phase velocity ω/k. Also note from Eqs. (6) and (7) that for a given frequency ω, the phase velocities of the left- and right-circularly-polarized radiation fields are $\omega/(k-k_0)$ and $\omega/(k+k_0)$, respectively. In particular, for $\omega > 0$, the left-circularly-polarized field propagates in the negative z-direction for $k < k_0$ (i.e., $\hat{k} < 1$), and in the positive z-direction for $k > k_0$ (i.e., $\hat{k} > 1$).

B. Polarization and Electromagnetic Energies

Solving the matrix equation (9) with the aid of the FDR [Eq. (20)], we obtain the following amplitude ratios

$$\frac{\phi_k}{A^-_{k-k_0}} = \frac{\hat{\omega}_c}{2}\,\frac{[\hat{D}^T_{k+k_0} + \hat{D}^T_{k-k_0}]}{\hat{D}^L_k \hat{D}^T_{k+k_0}}\,\hat{\chi}^{(1)}_k \quad ,$$

$$\frac{\phi_k}{A^+_{k+k_0}} = \frac{\hat{\omega}_c}{2}\,\frac{[\hat{D}^T_{k+k_0} + \hat{D}^T_{k-k_0}]}{\hat{D}^L_k \hat{D}^T_{k-k_0}}\,\hat{\chi}^{(1)}_k \quad , \tag{22}$$

and

$$\frac{A^-_{k+k_0}}{A^+_{k-k_0}} = \frac{\hat{D}^T_{k-k_0}}{\hat{D}^T_{k+k_0}} \quad .$$

For the special case of monochromatic perturbation with $|\mathrm{Im}(\hat{\omega})| << |\mathrm{Re}(\hat{\omega})|$, the electromagnetic energy density, averaged over one cycle, is given by

$$E = \frac{1}{2}\left[\frac{\underset{\sim}{\delta B}\cdot\underset{\sim}{\delta B}^*}{8\pi} + \frac{\underset{\sim}{\delta E}\cdot\underset{\sim}{\delta E}^*}{8\pi}\right] \quad . \tag{23}$$

The perturbed fields are

$$\underset{\sim}{\delta B} = \underset{\sim}{\nabla} \times \underset{\sim}{\delta A} \quad ,$$

and

$$\delta\underset{\sim}{E} = -\underset{\sim}{\nabla}\delta\phi - \frac{1}{c}\frac{\partial}{\partial t}\delta\underset{\sim}{A} ,$$

where $\delta\underset{\sim}{A} = (1/\sqrt{2})(\hat{\underset{\sim}{e}}_x + i\hat{\underset{\sim}{e}}_y)\delta A^{-}_{k-k_0} + (1/\sqrt{2})(\hat{\underset{\sim}{e}}_x - i\hat{\underset{\sim}{e}}_y)\delta A^{+}_{k+k_0}$, and $\delta\phi = \delta\phi_k$ [see Eqs. (6)-(8)].

From Eq. (23), it follows that the contributions to the longitudinal oscillations, the right-circularly-polarized radiation field, and the left-circularly-polarized radiation field to the total electromagnetic energy are separable. Denoting these contributions by $E_L(\hat{\omega},\hat{k})$, $E_+(\hat{\omega},\hat{k}+1)$ and $E_-(\hat{\omega},\hat{k}-1)$, respectively, and making use of Eq. (22), we obtain the electromagnetic energy ratios

$$\frac{E_L(\hat{\omega},\hat{k})}{E_+(\hat{\omega},\hat{k}+1)} = \frac{\hat{\omega}_c^2\hat{k}^2}{2[(\hat{k}+1)^2+|\hat{\omega}(\hat{k})|^2]}\left|\frac{[\hat{D}^T_{k+k_0}+\hat{D}^T_{k-k_0}]}{\hat{D}^L_k\hat{D}^T_{k-k_0}}\hat{\chi}^{(1)}_k\right|^2 , \qquad (24)$$

$$\frac{E_L(\hat{\omega},\hat{k})}{E_-(\hat{\omega},\hat{k}-1)} = \frac{\hat{\omega}_c^2\hat{k}^2}{2[(\hat{k}-1)^2+|\hat{\omega}(\hat{k})|^2]}\left|\frac{[\hat{D}^T_{k+k_0}+\hat{D}^T_{k-k_0}]}{\hat{D}^L_k\hat{D}^T_{k+k_0}}\hat{\chi}^{(1)}_k\right|^2 , \qquad (25)$$

and

$$\frac{E_+(\hat{\omega},\hat{k}+1)}{E_-(\hat{\omega},\hat{k}-1)} = \frac{[(\hat{k}+1)^2+|\hat{\omega}(\hat{k})|^2]}{[(\hat{k}-1)^2+|\hat{\omega}(\hat{k})|^2]}\left|\frac{\hat{D}^T_{k-k_0}}{\hat{D}^T_{k+k_0}}\right|^2 . \qquad (26)$$

The cold-fluid limits of the above energy ratios are used later in this paper.

C. The Compton Dispersion Relation

If the longitudinal potential $\delta\phi$ is neglected in the derivation of Eq. (9), then we obtain a two-dimensional matrix dispersion equation involving only the vector potentials $A^{\pm}_{k\pm k_0}$. We refer to the corresponding secular equation as the full Compton dispersion relation (CDR). The CDR is given by

$$\hat{D}^T_{k+k_0}\hat{D}^T_{k-k_0} = -\frac{1}{2}\hat{\omega}_c^2(\hat{D}^T_{k+k_0}+\hat{D}^T_{k-k_0})(\alpha_3\hat{\omega}_p^2+\hat{\chi}_k^{(2)}) \ . \tag{27}$$

D. Cold-Beam Dispersion Relations

In this paper, we deal with the FDR and CDR for the case of a cold electron beam. To obtain dispersion relations for a cold beam, the equilibrium distribution function is specified by $G_0(p_z)=\delta(p_z-p_0)$ in Eqs. (13) - (16). The resulting cold-beam FDR [Eq. (20)] is given by

$$\begin{aligned}&[(\hat{\omega}-\hat{k}\beta_b)^2-\hat{\omega}_p^2/\gamma_b^2][\hat{\omega}^2-(\hat{k}+1)^2-\hat{\omega}_p^2][\hat{\omega}^2-(\hat{k}-1)^2-\hat{\omega}_p^2]\\ &=-\hat{\omega}_c^2\hat{\omega}_p^2[\hat{\omega}^2-(\hat{k}^2+1)-\hat{\omega}_p^2][\hat{\omega}^2-\hat{k}^2-\hat{\omega}_p^2] \ .\end{aligned} \tag{28}$$

To obtain the above dispersion relation, we have set the constant $\bar{\gamma}$ [appearing in Eqs. (13) - (15) and (18) - (19)] equal to γ_0, where γ_0 is defined by

$$\gamma_0 mc^2 \equiv [m^2c^4+p_0^2c^2+e^2B_0^2/k_0^2]^{1/2} \ . \tag{29}$$

Moreover, the quantity γ_b is defined by

$$\gamma_b = (1-\beta_b^2)^{-1/2} \ , \tag{30}$$

where β_b, the ratio of the unperturbed axial beam velocity to the speed of light, is given by

$$\beta_b = \frac{p_0}{\gamma_0 mc} \ . \tag{31}$$

The quantities γ_0 and γ_b are related by the expression

$$\frac{1}{\gamma_b^2} = \frac{1}{\gamma_0^2} + \hat{\omega}_c^2 , \tag{32}$$

where $\hat{\omega}_c = (eB_0/\gamma_0 mc)/ck_0$, and $\gamma_0 > \gamma_b$ necessarily follows from Eqs. (29) - (32). We note that it is (incorrectly) assumed that $\gamma_b > \gamma_0$ in several of the cold-beam numerical calculations in Ref. 1. These nonphysical examples are those whose temporal growth rate curves fail to vanish above some finite value of the wavenumber. (See Figs. 2 and 5-11 of Ref. 1.)

The cold-beam CDR [obtained from Eq. (27)] is

$$\begin{aligned}&[\hat{\omega}-\hat{k}\beta_b]^2[\hat{\omega}^2-(\hat{k}+1)^2-\hat{\omega}_p^2][\hat{\omega}^2-(\hat{k}-1)^2-\hat{\omega}_p^2] \\ &\quad = -\hat{\omega}_c^2\hat{\omega}_p^2[\hat{\omega}^2-(\hat{k}^2+1)-\hat{\omega}_p^2][\hat{\omega}^2-\hat{k}^2].\end{aligned} \tag{33}$$

Comparing Eq. (33) with Eq. (28), we find that a condition for validity of the cold-beam CDR is that

$$|\hat{\omega}-\hat{k}\beta_b| >> \hat{\omega}_p/\gamma_b \quad . \tag{34}$$

Clearly, a second requirement for validity of the CDR is that $|\hat{\omega}^2-\hat{k}^2|>>\hat{\omega}_p^2$. However, it can be shown that Eq. (34) implies this second inequality if $\hat{\omega}_p/\gamma_b \lesssim 1$ and $\hat{k}^2 \geq \gamma_b^4$. Thus, Eq. (34) assures the validity of the Compton approximation at the upshifted peak for all systems of moderate density.

For the case of a cold beam, Eqs. (24) - (26) reduce to

$$\frac{E_L(\hat{\omega},\hat{k})}{E_+(\hat{\omega},\hat{k}+1)} = 2\,\frac{\hat{\omega}_c^2\hat{\omega}_p^4}{[(\hat{k}+1)^2+|\hat{\omega}|^2]}\left|\frac{[\hat{\omega}^2-\hat{k}^2-1-\hat{\omega}_p^2][\hat{\omega}\beta_b-\hat{k}]}{[\hat{\omega}^2-(\hat{k}-1)^2-\hat{\omega}_p^2][(\hat{\omega}-\hat{k}\beta_b)^2-\hat{\omega}_p^2/\gamma_b^2]}\right|^2 , \tag{35}$$

$$\frac{E_L(\hat{\omega},\hat{k})}{E_-(\hat{\omega},\hat{k}-1)} = 2\,\frac{\hat{\omega}_c^2\hat{\omega}_p^4}{[(\hat{k}-1)^2+|\hat{\omega}|^2]}\left|\frac{[\hat{\omega}^2-\hat{k}^2-1-\hat{\omega}_p^2][\hat{\omega}\beta_b-\hat{k}]}{[\hat{\omega}^2-(\hat{k}+1)^2-\hat{\omega}_p^2][(\hat{\omega}-\hat{k}\beta_b)^2-\hat{\omega}_p^2/\gamma_b^2]}\right|^2 , \tag{36}$$

and

$$\frac{E_+(\hat{\omega},\hat{k}+1)}{E_-(\hat{\omega},\hat{k}-1)} = \frac{[(\hat{k}+1)^2+|\hat{\omega}|^2]}{[(\hat{k}-1)^2+|\hat{\omega}|^2]}\left|\frac{\hat{\omega}^2-(\hat{k}-1)^2-\hat{\omega}_p^2}{\hat{\omega}^2-(\hat{k}+1)^2-\hat{\omega}_p^2}\right|^2 . \tag{37}$$

In Eqs. (35) - (37), the quantities $E_L(\hat{\omega},\hat{k})$, $E_-(\hat{\omega},\hat{k}-1)$ and $E_+(\hat{\omega},\hat{k}+1)$ are the electromagnetic energy densities associated with the longitudinal oscillations and the left- and right-hand circularly-polarized electromagnetic fields, respectively, for the case of a monochromatic wave perturbation with frequency $\hat{\omega}$.

It should be noted that both $E_L(\hat{\omega},\hat{k})/E_+(\hat{\omega},\hat{k}+1)$ and $E_L(\hat{\omega},\hat{k})/E_-(\hat{\omega},\hat{k}-1)$ approach infinity as $(\hat{\omega}-\hat{k}\beta_b)^2 \rightarrow \hat{\omega}_p^2/\gamma_b^2$. On the other hand, non-zero electrostatic energy remains in the longitudinal plasma oscillations as $\hat{\omega}^2 \rightarrow (\hat{k}\pm 1)^2 + \hat{\omega}_p^2$.

III. PROPERTIES OF THE COLD-BEAM DISPERSION RELATION

The cold-beam full dispersion relation FDR [Eq. (28)] is a sixth-degree polynomial in $\hat{\omega}$. Thus, complex roots of the FDR will occur in complex conjugate pairs, one of which will represent growth, when $\mathrm{Im}(\hat{\omega})>0$. The occurrence of complex roots can be analyzed[2] by writing the cold-beam FDR in the form

$$\mathrm{LHS} = \mathrm{RHS} \ , \tag{38}$$

where LHS is the parabola defined by LHS = $(\hat{\omega}-\hat{k}\beta_b)^2 - \hat{\omega}_p^2/\gamma_b^2$, and RHS is the discontinuous curve

$$\mathrm{RHS} = -\hat{\omega}_c^2\hat{\omega}_p^2 \frac{[\hat{\omega}^2-\hat{\omega}_2^2][\hat{\omega}^2-\hat{\omega}_1^2]}{[\hat{\omega}^2-\hat{\omega}_+^2][\hat{\omega}^2-\hat{\omega}_-^2]} \ .$$

Here we have defined the frequencies

$$\hat{\omega}_1 = (\hat{k}^2+\hat{\omega}_p^2)^{1/2} \ , \tag{39}$$

$$\hat{\omega}_2 = (\hat{k}^2+1+\hat{\omega}_p^2)^{1/2} \ , \tag{40}$$

$$\hat{\omega}_+ = [(\hat{k}+1)^2+\hat{\omega}_p^2]^{1/2} \ , \tag{41}$$

and

$$\hat{\omega}_- = [(\hat{k}-1)^2+\hat{\omega}_p^2]^{1/2} \ . \tag{42}$$

For $\hat{k} \geq 0$, these frequencies satisfy the orderings

$$\hat{\omega}_+ > \hat{\omega}_2 > \hat{\omega}_1 > \hat{\omega}_- \ , \ \text{for } \hat{k} > \frac{1}{2} \ , \tag{43}$$

and

$$\hat{\omega}_+ > \hat{\omega}_2 > \hat{\omega}_- > \hat{\omega}_1 \ , \ \text{for } 0 < \hat{k} < \frac{1}{2} \ . \tag{44}$$

Graphs of LHS and RHS versus real $\hat{\omega}$ for fixed $\hat{k}$ are shown schematically in Figs. 1(a) and 1(b) for $0 < \hat{k} < 1/2$ and $\hat{k} > 1/2$, respectively. For the values of $\hat{k}$ shown, there are six real roots and no complex roots of the FDR because the LHS and RHS curves are shown to have six intersections. Additional frequencies shown on the graphs are

$$\hat{\omega}_u = \hat{k}\beta_b + \hat{\omega}_p/\gamma_b \ , \tag{45}$$

and

$$\hat{\omega}_\ell = \hat{k}\beta_b - \hat{\omega}_p/\gamma_b \ , \tag{46}$$

which are the positive- and negative-energy longitudinal space-charge wave frequencies, respectively. The occurrence of complex roots $\hat{\omega}$ of the FDR for positive $\hat{k}$ can be determined by considering the manner in which the graphs in Figs. 1(a) and 1(b) change as $\hat{k} \geq 0$ varies. Consider the behavior of the quantity $\hat{\omega}_u - \hat{\omega}_1$. Using Eqs. (39) and (45), we find that $\hat{\omega}_u - \hat{\omega}_1 = -\hat{\omega}_p(1-1/\gamma_b) < 0$, at $\hat{k}=0$. The quantity $\hat{\omega}_u - \hat{\omega}_1$ attains a maximum value of zero at $\hat{k} = \hat{\omega}_p\gamma_b\beta_b$ (where $\hat{\omega}=\hat{\omega}_u$ is a real root of the FDR), and then approaches $-\infty$ as $\hat{k}$ approaches $+\infty$.

With the aid of Fig. 1(a), we find that the FDR has six real roots (and therefore exhibits no instability) for all $\hat{k}$ in the interval $0 < \hat{k} < 1/2$ by using the following argument. Making use of Eq. (38), it is easily shown that RHS $(\hat{\omega}, \hat{k})$ is a monotonically increasing function of $\hat{\omega}$ for $0 \leq \hat{\omega} < \hat{\omega}_1$ provided $0 \leq \hat{k} < 1/2$. The minimum of RHS at $\hat{\omega} = 0$ is given by

$$\mathrm{RHS}(0,\hat{k}) = -\hat{\omega}_c^2\hat{\omega}_p^2 \frac{\hat{\omega}_1^2}{\hat{\omega}_-^2}\frac{\hat{\omega}_2^2}{\hat{\omega}_+^2} , \tag{47}$$

whereas the minimum of the parabola is $-\hat{\omega}_p^2/\gamma_b^2$. According to the inequality in Eq. (44), $|\mathrm{RHS}(0,\hat{k})| < \hat{\omega}_c^2\hat{\omega}_p^2$, whereas it follows from Eq. (32) that

$$\hat{\omega}_p^2/\gamma_b^2 = \hat{\omega}_p^2\left(\frac{1}{\gamma_0^2} + \hat{\omega}_c^2\right) > \hat{\omega}_p^2\hat{\omega}_c^2 .$$

It was noted in the preceding paragraph that $\hat{\omega}_u \leq \hat{\omega}_1$. Therefore, the FDR has two real roots in the interval $0 \leq \hat{\omega} < \hat{\omega}_-$ and four elsewhere, for a total of six. For the FDR, it therefore follows that $\mathrm{Im}(\hat{\omega})=0$ for $\hat{k}$ in the interval $0 < \hat{k} < 1/2$.

Next we consider the case where $\hat{k} > 1/2$. We give here a qualitative description of how the complex roots of the FDR appear and disappear as $\hat{k}$ ranges from 1/2 to infinity. Mathematical details are given later in this section. Referring to Fig. 1(b), we note that all of the quantities $\hat{\omega}_\ell$, $\hat{k}\beta_b$, $\hat{\omega}_u$, $\hat{\omega}_-$, $\hat{\omega}_1$, $\hat{\omega}_2$, and $\hat{\omega}_+$ increase with increasing $\hat{k}$. However, the parabola (LHS) at first shifts to the right relative to the RHS curve, for increasing $\hat{k}$. Then, with further increase in $\hat{k}$, the parabola shifts back to the left. If the parabola shifts sufficiently far to the right, it will no longer intersect with that portion of the RHS curve between 0 and $\hat{\omega}_-$ in Fig. 1(b), and two complex conjugate roots of the FDR will appear. The parabola may then shift back to the left. As a result, a plot of $\mathrm{Im}(\hat{\omega})$ versus $\hat{k}$ will exhibit a single growth interval where $\mathrm{Im}(\hat{\omega}) > 0$ [see Fig. 3(a)]. A second possibility is that the parabola shifts sufficiently far to the right that it intersects the RHS curve in the interval $\hat{\omega}_- < \hat{\omega} \leq \hat{\omega}_1$ as shown in Fig. 2. Then a plot of $\mathrm{Im}(\hat{\omega})$ versus $\hat{k}$ will exhibit two growth intervals, the first being produced as the parabola shifts to the right and the second as it shifts back to the left. We refer to these as the <u>downshifted</u> and <u>upshifted</u> peaks, respectively [see Fig. 3(b)]. Since $\hat{\omega}_u \leq \hat{\omega}_1$, the parabola will always intersect that portion of the RHS curve in the interval $\hat{\omega}_- < \hat{\omega} < \hat{\omega}_+$. Thus, the FDR has at most two complex roots, one of which corresponds to growth $[\mathrm{Im}(\hat{\omega})>0]$.

The mathematical details justifying the above description are the following. Making use of Eq. (42), one can easily show that the quantity $(\hat{k}\beta_b-\hat{\omega}_-)$ increases monotonically with increasing $\hat{k}$ from the value $-\hat{\omega}_p$ at $\hat{k}=0$, to a maximum value of $\beta_b-\hat{\omega}_p/\gamma_b$ at $\hat{k}=1+\beta_b\gamma_p\hat{\omega}_p$. With a further increase in $\hat{k}$, the quantity $(\hat{k}\beta_b-\hat{\omega}_-)$ decreases monotonically approaching $-\infty$ as $\hat{k}$ approaches $+\infty$. Further, if we evaluate RHS at $\hat{\omega}=\hat{k}\beta_b$ (the position of the minimum of the parabola) and let $\hat{k}\to\infty$, we find

$$\lim_{\hat{k}\to\infty} \mathrm{RHS}(\hat{k}\beta_b,\hat{k})=-\hat{\omega}_c^2\hat{\omega}_p^2 \ .$$

Since $\hat{\omega}_c^2\hat{\omega}_p^2 < \hat{\omega}_p^2/\gamma_b^2$ = the distance of the minimum of the parabola below the real $\hat{\omega}$-axis, we find that the parabola must intersect the RHS curve between 0 and $\hat{\omega}_-$ for all $\hat{k}$ larger than some finite value. Therefore, there is some finite value of $\hat{k}$ beyond which $\mathrm{Im}(\hat{\omega}) = 0$.

The boundaries of the growth peak (or peaks) in a plot of $\mathrm{Im}(\hat{\omega})$ versus $\hat{k}$ are those values of $\hat{k}$ for which LHS and RHS versus $\hat{\omega}$ have points of tangency; that is, those real values of $\hat{k}$ which obey the two equations LHS=RHS and $\partial\mathrm{LHS}/\partial\omega=\partial\mathrm{RHS}/\partial\omega$. However, we have had little success in obtaining analytic solutions to these equations. Upper and lower bounds

($\hat{k}_{ub}$ and $\hat{k}_{\ell b}$) of the entire growth region, however, can be obtained as follows. Referring to Fig. 1(b) and assuming that the parabola shifts to the right (with increasing $\hat{k}$) relative to the RHS curve, we note that $\omega=\hat{k}\beta_b$ will become a root of the FDR before the left-most boundary of a growth peak in a plot of $\mathrm{Im}(\hat{\omega})$ versus $\hat{k}$ is reached. Then, assuming that the parabola shifts to the left with increasing $\hat{k}$, we find that $\hat{\omega}=\hat{k}\beta_b$ again becomes a root, after the right-most boundary of a growth peak is attained. Substituting $\hat{\omega}=\hat{k}\beta_b$ into the FDR and solving for $\hat{k}$, we obtain the solutions

$$\left.\begin{matrix}\hat{k}^2_{ub}\\ \hat{k}^2_{\ell b}\end{matrix}\right\} = \frac{1}{2}\,[-b\pm(b^2-4c)^{1/2}]\ , \tag{48}$$

where

$$b = -[4\gamma_b^2\gamma_0^2 - 2\gamma_b^2\hat{\omega}_p^2 - \gamma_0^2 - \gamma_b^2],$$

and

$$c = (1+\hat{\omega}_p^2)\gamma_b^2[\gamma_0^2+\hat{\omega}_p^2\gamma_b^2]\ .$$

Thus, $\hat{k}_{ub} > 0$ and $\hat{k}_{\ell b} > 0$ provide upper and lower bounds respectively on the entire growth region for nonnegative $\hat{k}$ as shown in Figs. 3(a) and 3(b). (For a high-energy beam satisfying $\gamma_0 >> 1$, $\gamma_b >> 1$ and $\hat{\omega}_p \lesssim 1$, it follows that $\hat{k}_{ub} \simeq 2\gamma_b\gamma_0$.)

In the numerical analysis, we often find that $\hat{k}_{ub}$ and $\hat{k}_{\ell b}$ provide excellent approximations to the upper and lower boundaries of the growth region. This situation occurs when the RHS curve between 0 and $\hat{\omega}_-$ does not deviate appreciably from the horizontal at its point of tangency with the parabola. On the other hand, we find numerically that $\hat{k}_{ub}$

and $\hat{k}_{\ell b}$ are poor (but still useful) approximations to the boundaries of the instability region if the point of tangency of the LHS parabola with the RHS curve for $0 < \hat{\omega} < \hat{\omega}_-$ occurs close to $\hat{\omega}_-$, where the magnitude of the slope of the RHS curve is relatively large.

Upper and lower bounds ($\hat{k}'_{ub}$ and $\hat{k}'_{\ell b}$) on the interval between the downshifted and upshifted peaks can be obtained by noting that with increasing $\hat{k}$, $\hat{\omega}_\ell$ coincides with $\hat{\omega}_-$ before the situation depicted in Fig. 2 occurs and coincides again with $\hat{\omega}_-$ after the situation ceases to occur. Setting $\hat{\omega}_\ell = \hat{\omega}_-$ and solving for $\hat{k}$, with the aid of Eqs. (42) and (46), we obtain

$$\left.\begin{matrix} \hat{k}'_{ub} \\ \hat{k}'_{\ell b} \end{matrix}\right\} = \gamma_b^2 \left\{ \left(1 - \frac{\beta_b \hat{\omega}_p}{\gamma_b}\right) \pm \left(\beta_b^2 - \frac{2\beta_b \hat{\omega}_p}{\gamma_b}\right)^{1/2} \right\} . \tag{49}$$

The quantities $\hat{k}'_{ub}$ and $\hat{k}'_{\ell b}$ are upper and lower bounds, respectively, on the interval between the unstable $\hat{k}$-ranges.

Equation (49) is normally used in the literature to estimate positions of the maxima of the upshifted and downshifted peaks and not to bound the interval between the unstable $\hat{k}$-ranges. From our numerical studies, we find that if two well defined peaks are present, Eq. (49) gives better estimates of the maxima of $\mathrm{Im}(\hat{\omega})$ than of the actual marginal stability boundaries. Nevertheless, Eq. (49) does provide us with a sufficient condition that no interval with $\mathrm{Im}(\hat{\omega})=0$ exists [as in Fig. 3(a)]. Clearly, real solutions for $\hat{k}'_{ub}$ and $\hat{k}'_{\ell b}$ do not exist if the discriminant in Eq. (49) is negative. Thus, the upshifted and downshifted unstable regions will overlap provided

$$\hat{\omega}_p \geq \frac{\gamma_b \beta_b}{2} . \tag{50}$$

In Fig. 4, we plot the minimum $\hat{\omega}_p (=\gamma_b \beta_b/2)$ for which the inequality in Eq. (50) holds versus γ_b. Note that if $\hat{\omega}_p < 1$, then the sufficiency condition is satisfied only if $\gamma_b < 2.3$. Of course, unstable regions can overlap before the sufficiency condition is satisfied.

The discussion in this section is concerned mainly with the behavior of two of the six branches $\hat{\omega}(\hat{k})$ of the cold-beam FDR, namely, those two branches which become complex conjugates in the unstable $\hat{k}$-intervals. The large-$\hat{k}$ behavior of the two branches is given by

$$\hat{\omega} \to \hat{k}\beta_b \pm \left(\frac{\hat{\omega}_p^2}{\gamma_b^2} - \hat{\omega}_c^2 \hat{\omega}_p^2 \right)^{1/2} = \hat{k}\beta_b \pm \frac{\hat{\omega}_p}{\gamma_0} . \tag{51}$$

The above result is obtained by co-locating the intersections of the parabola in Fig. 3(a), with the horizontal line RHS $\to -\hat{\omega}_c^2 \hat{\omega}_p^2$ as $\hat{k} \to \infty$, $0 < \hat{\omega} < \hat{\omega}_-$. Equation (51) shows that these branches become longitudinal plasma oscillations for large $\hat{k}$, provided that $\gamma_b \simeq \gamma_0$. However, for a sufficiently large wiggler field, γ_0 may differ significantly from γ_b [as evident from Eq. (32)] and an appreciable amount of the energy in these branches may be contained in the radiation fields at large $\hat{k}$. In the limit of large $\hat{k}$ for these two branches, the energy ratios in Eqs. (35) and (36) become

$$\lim_{\hat{k}\to\infty} \frac{E_L(\hat{\omega},\hat{k})}{E_+(\hat{\omega},\hat{k}+1)} = \lim_{\hat{k}\to\infty} \frac{E_L(\hat{\omega},\hat{k})}{E_-(\hat{\omega},\hat{k}+1)} = \frac{2}{\hat{\omega}_c^2\gamma_b^4(1+\beta_b^2)} . \quad (52)$$

IV. A COLD-BEAM STABILITY CRITERION

Equation (48) gives upper and lower bounds ($\hat{k}_{ub}$ and $\hat{k}_{\ell b}$) on the entire unstable $\hat{k}$-region for the case of a cold beam. Thus, if distinct, real $\hat{k}_{ub}$ and $\hat{k}_{\ell b}$ do not exist, then there will be no growth region. It follows from Eq. (48) that a sufficient condition for the full dispersion relation (FDR) in Eq. (28) to give stable solutions ($\text{Im}\hat{\omega}=0$) for all $\hat{k}$ is

$$b^2 \le 4c.$$

This stability condition can be written in the form

$$\hat{\omega}_p^2 \ge \gamma_0^2 + \frac{1}{16\gamma_0^2} + \frac{1}{16}\frac{\gamma_0^2}{\gamma_b^4} - \frac{1}{2}\left(1 + \frac{\gamma_0^2}{\gamma_b^2} + \frac{1}{4\gamma_b^2}\right) \equiv [\hat{\omega}_p^2]_{\text{MIN}} . \quad (53)$$

A free electron laser for which the cold-beam FDR [Eq. (28)] is applicable will become stable at sufficiently high beam densities. However, for moderate densities ($\hat{\omega}_p^2 \lesssim 1$), the above inequality is not satisfied except for beams with low values of γ_0.

Figure 5 shows contours of constant $[\hat{\omega}_p^2]_{\text{MIN}}$ in (γ_0,γ_b) space. Referring to Eq. (32), we note that $\hat{\omega}_c^2 = 0$ on the diagonal ($\gamma_b = \gamma_0$) and that $\hat{\omega}_c^2$ attains a maximum value of $\hat{\omega}_c^2 = (\gamma_0^2-1)/\gamma_0^2$ on the γ_0-axis. For $\hat{\omega}_p^2 \ge [\hat{\omega}_p^2]_{\text{MIN}}$, the system is stable for all values of γ_0 and γ_b below the corresponding contour in Fig. 5.

The condition $\hat{\omega}_p \geq \gamma_b\beta_b/2$ [Eq. (50)] is sometimes given as an approximate cold-beam stability criterion.[3] However, this condition bears little similarity to the inequality in Eq. (53). For example, contours of constant $\gamma_b\beta_b/2$ appear as vertical lines in Fig. 5. In Sec. VII, we investigate an example of a system satisfying the inequality in Eq. (50) which exhibits a large growth rate. In the limit $\gamma_b=\gamma_0$, the inequality in Eq. (53) reduces to $\hat{\omega}_p \geq \gamma_b\beta_b$.

Figure 6 gives numerical results obtained from the FDR [Eq. (28)] illustrating the onset of stability, with increasing $\hat{\omega}_p^2$, for fixed $\gamma_0=1.3$ and $\gamma_b=1.1$. The sufficient condition for stability [Eq. (53)] is satisfied by all $\hat{\omega}_p^2 \geq 0.498$. On the other hand, our numerical analysis shows that instability ceases when $\hat{\omega}_p^2 \geq 0.37$.

V. PROPERTIES OF THE COLD-BEAM COMPTON DISPERSION RELATION

The analysis of the cold-beam Compton Dispersion Relation (CDR) is analogous to that of the FDR in Eq. (28). We express the CDR in the form

$$\mathrm{LHS} = \mathrm{RHS} \tag{54}$$

where

$$\mathrm{LHS} = [\hat{\omega}-\hat{k}\beta_b]^2 \ ,$$

and

$$\mathrm{RHS} = -\hat{\omega}_c^2\hat{\omega}_p^2 \, \frac{[\hat{\omega}^2-\hat{\omega}_2^2][\hat{\omega}^2-\hat{k}^2]}{[\hat{\omega}^2-\hat{\omega}_+^2][\omega^2-\hat{\omega}_-^2]} \ .$$

The frequencies appearing in the above definitions are

$$\hat{\omega}_+ = [(\hat{k}+1)^2+\hat{\omega}_p^2]^{1/2} \tag{55}$$

$$\hat{\omega}_- = [(\hat{k}-1)^2+\hat{\omega}_p^2]^{1/2} \tag{56}$$

and

$$\hat{\omega}_2 = (\hat{k}^2+1+\hat{\omega}_p^2) \ , \tag{57}$$

where the following orderings are satisfied

$$\hat{\omega}_+ > \hat{\omega}_2 > \hat{k} > \hat{\omega}_1 \ , \ \text{if } \hat{k} > \frac{1+\hat{\omega}_p}{2} \ ,$$

and

$$\hat{\omega}_+ > \hat{\omega}_2 > \hat{\omega}_- > \hat{k} \ , \quad \text{if } 0 < \hat{k} < \frac{1+\hat{\omega}_p}{2} \ .$$

Schematic plots of LHS and RHS versus $\hat{\omega}$, for fixed $\hat{k}$, are shown in Figures 7(a) and 7(b) for the cases where $0<\hat{k}<\hat{\omega}_p/2$, and $\hat{k}>\hat{\omega}_p/2$, respectively.

It is evident from Fig. 7(a) that the CDR has exactly two complex conjugate roots (one of which represents growth) for all $\hat{k}$ in the interval $0 < \hat{k} < (1+\hat{\omega}_p)/2$. Referring to Eq. (33) for the CDR, we see that these complex conjugate roots reduce to a double root at $\hat{\omega}=0$ for $\hat{k}=0$. The behavior of the complex conjugate branches of the CDR for small $\hat{k}>0$ is determined by neglecting all powers of $\hat{\omega}$ higher than quadratic in Eq. (33) and solving for $\hat{\omega}$ to linear order in $\hat{k}$. The result is

$$\hat{\omega} = \frac{\hat{k}\beta_b(1+\hat{\omega}_p^2)}{[(1+\hat{\omega}_p^2)-\hat{\omega}_c^2\hat{\omega}_p^2]} \pm \frac{i\hat{k}\hat{\omega}_c\hat{\omega}_p(1/\gamma_b^2+\hat{\omega}_p^2/\gamma_0^2)^{1/2}}{[(1+\hat{\omega}_p^2)-\hat{\omega}_c^2\hat{\omega}_p^2]} \quad . \tag{58}$$

It follows that a plot of $\mathrm{Im}(\hat{\omega})$ versus $\hat{k} \geq 0$ for the unstable branch gives zero growth rate at $\hat{k}=0$, increases linearly in the neighborhood of $\hat{k}=0$, and remains positive over the interval $0 < \hat{k} < (1+\hat{\omega}_p)/2$. Also note that the phase velocity $\mathrm{Re}(\hat{\omega})/k$ is greater than β_b in this small-$\hat{k}$ growth region.

The treatment of the CDR for $\hat{k} > (1+\hat{\omega}_p)/2$ is somewhat similar to that of the FDR for $\hat{k} > 1/2$. As shown in Sec. III, the quantity $(\hat{k}\beta_b-\hat{\omega}_-)$ increases monotonically with increasing $\hat{k}$, from the value $-\hat{\omega}_p$ at $\hat{k}=0$, to a maximum value of $(\beta_b-\hat{\omega}_p/\gamma_b)$ at $\hat{k}=1+\beta_b\hat{\omega}_p\gamma_b$. Then, as $\hat{k}\to\infty$, the quantity $(\hat{k}\beta_b-\omega_-)$ decreases monotonically to $-\infty$. The process can be pictured as a shift to the right of the LHS parabola relative to the RHS curve in Fig. 7(b), followed by a relative shift back to the left. If, as a result of this process, the parabola fails to form additional intersections with the RHS curve [in addition to the original four depicted in Fig. 7(b)], then the cold-beam CDR exhibits instability for all $\hat{k}> 0$. However, an interval of no growth will exist over a finite interval of $\hat{k}$ if the situation shown in Fig. 8 exists over that interval.

The CDR will then be unstable in two regions of $\hat{k}$-space. The first region will extend from $\hat{k}=0$ to the lowest value of $\hat{k}$ for which the parabola is tangential to the RHS curve in the interval $\hat{\omega}_- < \hat{\omega} < \hat{k}$. The second region will extend to infinity from the larger value of $\hat{k}$ for which there is a tangency.

Since $\hat{k}\beta_b < \hat{k}$, the LHS parabola always has two intersections with the RHS curve in the interval $\hat{\omega}_- < \hat{\omega} < \hat{\omega}_+$ [see Fig. 7(b)], Thus, the cold-beam CDR in Eq. (33) has at most two complex roots, one of which corresponds to growth ($\text{Im}\hat{\omega}>0$).

The discussion in this section is concerned with those two of the six branches of the CDR which are complex conjugates in the unstable $\hat{k}$-regions. The behavior of these branches for large $\hat{k}$ can be determined by letting $\hat{k}\to\infty$ in the RHS of Eq. (54), and solving for $\hat{\omega}$. We obtain

$$\hat{\omega} \to \hat{k}\beta_b \pm i\hat{\omega}_c\hat{\omega}_p \ . \tag{59}$$

Therefore, in a plot of $\text{Im}(\hat{\omega})$ versus k for the CDR, $\text{Im}(\hat{\omega})$ approaches the asymptote $\text{Im}(\hat{\omega})=\hat{\omega}_c\hat{\omega}_p$ as $\hat{k}$ approaches infinity.

The behavior of the cold-beam CDR growth rate curves discussed in this section is shown schematically in Figs. 3(a) and 3(b).

VI. CONDITION FOR VALIDITY OF THE COMPTON APPROXIMATION

From the discussion in Secs. III-V, it is clear that the cold-beam FDR [Eq. (28)] and CDR [Eq. (33)] are qualitatively different for both small and large values of $\hat{k}$ and that the Compton approximation is not valid in those limits. On the other hand, the two treatments are qualitatively similar for those values of $\hat{k}$ in the region of maximum growth. We adopt the following criterion for the validity of the Compton approximation. We compute the growth rate at the maxima of the (upshifted) peaks for the FDR and CDR, using Eqs. (28) and (33), respectively. If these values agree to within 5% of the FDR value, and the corresponding real parts of $\hat{\omega}$ also agree to within 5%, then we consider the Compton approximation to be valid. If not, but both of the above quantities agree to within 10%, then we consider the Compton approximation to be marginally valid. In either case, we refer to the system as a Compton system. All other systems are classified as Raman.

Cold-beam systems governed by the FDR or CDR are characterized by the three parameters γ_0, $\hat{\omega}_c$, and $\hat{\omega}_p$. Strictly speaking, an exhaustive study of the validity of the Compton approximation for cold beams would require a determination of the region in a three-dimensional parameter space in which the approximation is valid. We reduce the parameter space from three to two dimensions in the following way. First, we use a procedure similar to that of Kroll and McMullin[4,5] to obtain a condition for validity of the Compton approximation for cold beams in the neighborhood of the upshifted peak. If it is assumed that $\hat{D}^T_{k-k_0}(\hat{\omega}) \simeq 0$ and $\hat{D}^T_{k+k_0}(\hat{\omega}) \neq 0$ in Eq. (27), then the cold-beam CDR [Eq. (33)] is given approximately by

$$(\hat{\omega}-\hat{k}\beta_b)^2(\hat{\omega}^2-\hat{\omega}_-^2) = -\frac{1}{2}\hat{\omega}_c^2\hat{\omega}_p^2(\hat{\omega}^2-\hat{k}^2) \quad , \qquad (60)$$

where $\hat{\omega}_{-}^{2}=(\hat{k}-1)^{2}-\hat{\omega}_{p}^{2}$. Assuming that $\hat{\omega}\simeq\hat{k}\beta_{b}\simeq\hat{\omega}_{-}$ at the upshifted peak, we find that the solution to Eq. (60) corresponding to growth ($\mathrm{Im}\hat{\omega}>0$) is given approximately by

$$\hat{\omega} - \hat{k}\beta_{b} = \left(\frac{\hat{\omega}_{c}^{2}\hat{\omega}_{p}^{2}\hat{k}}{4\gamma_{b}^{2}\beta_{b}}\right)^{1/3}\left(-\frac{1}{2}+\frac{i\sqrt{3}}{2}\right) . \qquad (61)$$

A condition for validity of the CDR is $|\hat{\omega}-\hat{k}\beta_{b}|\gg\hat{\omega}_{p}/\gamma_{b}$ [Eq. (34)]. Substituting the approximate solution (61), one obtains the validity condition

$$\frac{\gamma_{b}\hat{k}}{4\beta_{b}} \gg \frac{\hat{\omega}_{p}}{\hat{\omega}_{c}^{2}} . \qquad (62)$$

If we approximate $\hat{k}$ at the upshifted peak maximum by $\hat{k}\simeq 1/(1-\beta_{b})$, then the condition for validity of the cold-beam Compton approximation can be expressed as

$$y \gg 4\sqrt{x}\sqrt{1-x}\,(1-\sqrt{1-x}) , \qquad (63)$$

where

$$x = \frac{1}{\gamma_{0}^{2}} + \hat{\omega}_{c}^{2} = \frac{1}{\gamma_{b}^{2}} ,$$

and

$$y = \frac{\hat{\omega}_{c}^{2}}{\hat{\omega}_{p}} .$$

By numerically determining the roots of the FDR and CDR [Eqs. (28) and (33)], we have classified a large number of systems as Compton, marginally Compton, and Raman according to the criteria established earlier in this section.

We find that the solid curve $y = 25\sqrt{x}\sqrt{1-x}(1-\sqrt{1-x})$, shown in Figs. 9(a) and 9(b), separates the Raman region of the two-dimensional parameter space from the Compton and marginally Compton regions. Moreover, the dashed curve $y=70\sqrt{x}\sqrt{1-x}(1-\sqrt{1-x})$, shown in Figs. 9(a) and 9(b), separates the Compton and marginally Compton regions. Thus, we adopt the condition

$$y > 25\sqrt{x}\sqrt{1-x}(1-\sqrt{1-x}) \ ,$$

where $y=\hat{\omega}_c^2/\hat{\omega}_p$ and $x=1/\gamma_b^2$, as the numerically-deduced validity condition for the cold-beam Compton approximation. If a system satisfies this condition, the Compton approximation, at maximum growth of the upshifted peak, will be valid [for both $\mathrm{Re}(\hat{\omega})$ and $\mathrm{Im}(\hat{\omega})$] to within an accuracy of approximately 10%. This validity criterion can be expressed in the equivalent form

$$\left(\frac{\omega_p c k_0}{\omega_c^2}\right) < \frac{\gamma_b^3}{25} \ \frac{(1+\beta_b)}{\beta_b} \quad . \tag{64}$$

Details of the above analysis are given in the Appendix A.

It is interesting to note that for fixed $\hat{\omega}_c^2/\hat{\omega}_p$, the Compton approximation becomes valid both in the limit of large γ_b, and in the limit that γ_b approaches unity. The latter results follow directly from Eq. (62), since $\hat{k}$ must be greater than 1/2 for growth to occur.

VII. THE RAMAN APPROXIMATION

In this paper, the term Raman is used to designate any system for which the Compton approximation is not valid. In a more restricted sense, a system is considered to satisfy the Raman approximation if its upshifted growth peak is due to a coupling of the negative-energy longitudinal wave and the left-hand polarized radiation field through the presence of the wiggler field. In such a case $\hat{\omega}_\ell \simeq \hat{\omega}_-$, $|\hat{\omega}-\hat{\omega}_u| >> |\hat{\omega}-\hat{\omega}_\ell|$ and $|\hat{\omega}-\hat{\omega}_-|$ at the maximum growth peak. In the following, we apply this approximation to the FDR [Eq. (28)].

The cold-beam Raman approximation, corresponding to that derived by Kwan et al[6,7] for the fluid case, is the following. We express the FDR in the form

$$[\hat{\omega}-\hat{\omega}_\ell][\hat{\omega}-\hat{\omega}_u][\hat{\omega}-\hat{\omega}_-] = R(\hat{\omega},\hat{k}) \ , \tag{65}$$

and make the approximation $R(\hat{\omega},\hat{k}) \simeq R(\hat{\omega}_-,\hat{k}) \equiv R$, where

$$R = \hat{\omega}_c^2 \hat{\omega}_p^2 (2\hat{k}-1)/4\hat{\omega}_- . \tag{66}$$

It is also assumed that

$$[\hat{\omega}-\hat{\omega}_u] \simeq [\hat{\omega}_\ell-\hat{\omega}_u] = -2L \ , \tag{67}$$

where $L=\hat{\omega}_p/\gamma_b$. Solving the resulting quadratic equation, we obtain the solution

$$\hat{\omega}-\hat{\omega}_- \simeq \frac{1}{2} [-\mu+i(2R/L-\mu^2)^{1/2}] \ , \tag{68}$$

for the unstable branch. Here $\mu = (\hat{\omega}_- - \hat{\omega}_\ell)$ is the frequency mismatch. We refer to Eq. (68) as the Raman approximation (RA).

A validity condition for the Raman approximation [Eq. (68)] is obtained by following the procedure of Kroll and McMullin.[3,4]

For the case of maximum growth (μ=0), Eq. (68) reduces to

$$\hat{\omega} \simeq \hat{\omega}_- + \frac{i}{2}\left(\frac{2R}{L}\right)^{1/2} . \tag{69}$$

At the growth maximum for a Raman system, it follows that

$$\hat{\omega}_- \simeq \hat{\omega}_\ell = \hat{k}\beta_b - L . \tag{70}$$

Consistency of Eqs. (67), (69), and (70) requires that

$$\left(\frac{2R}{L}\right)^{1/2} << 4L . \tag{71}$$

VIII. NUMERICAL ANALYSIS OF COMPTON AND RAMAN SYSTEMS

In this section we present detailed numerical solutions to the FDR [Eq. (28)] and the CDR [Eq. (33)] for three choices of cold-beam parameters, in order to illustrate several of the analytic results and stability properties described in the preceding sections. One of the systems is classified as Compton and two of the systems as Raman.

We also present numerical plots of the frequency mismatches $|\hat{\omega}-\hat{\omega}_1|$, $|\hat{\omega}-\hat{\omega}_-|$ $|\hat{\omega}-\hat{\omega}_u|$, $|\hat{\omega}-\hat{k}\beta_b|$ and $|\hat{\omega}-\hat{\omega}_+|$ as functions of $\hat{k}$ over the range of the (upshifted) peaks. Assumptions concerning the magnitudes of these mismatches are the basis of such approximations as Eqs. (33), (61), and (68). An interesting property of the results is that, in some cases, the relative values of the mismatches may vary significantly over the range of the peak. Thus, an approximation which predicts the maximum growth rate accurately may not necessarily give the correct detailed shape for $\mathrm{Im}(\hat{\omega})$ versus $\hat{k}$.

A. Example 1 (γ_0=2.0, $\hat{\omega}_p$=0.01, $\hat{\omega}_c$=0.5) - Compton System

In Figs. 10(a) and 10(b), we present numerical solutions to the CDR and FDR for the downshifted and upshifted growth rate curves, respectively, for a typical system classified as Compton according to the terminology in Sec. VI. The system parameters are γ_0=2.0, $\hat{\omega}_p$=0.01, and $\hat{\omega}_c$=0.5. It is located outside of the range of Fig. 9(b) with $1/\gamma_b^2$=0.5 and $\hat{\omega}_c^2/\hat{\omega}_p$=25. Referring to Figs. 10(a) and 10(b), it is evident that the respective upper and lower bounds on the FDR growth region [$\hat{k}_{ub}$ and $\hat{k}_{\ell b}$ given by Eq. (48)] are very good approximations to the boundaries of the FDR growth region. Moreover, the respective upper and lower bounds on the gap between the FDR peaks [$\hat{k}'_{ub}$ and $\hat{k}'_{\ell b}$ as given in Eq. (49)] are found to provide good approximations to the respective maxima of the peaks. (Recall that $\hat{k}'_{ub}$ and $\hat{k}'_{\ell b}$ are obtained by setting the frequency of the negative-energy longitudinal oscillations equal to the frequency of the forward-scattered radiation field.) A prominent feature of the FDR upshifted growth curve is the tail extending from the growth rate maximum in the direction of increasing $\hat{k}$. This feature will be discussed later in Sec. IX.

From Figs. 10(a) and 10(b), in agreement with the discussion in Sec. VI, the CDR growth rate curve provides an adequate approximation to that of the FDR only over the interval of $\hat{k}$ extending from the downshifted peak to somewhat beyond the maximum of the upshifted peak. In accordance with the discussion in Sec. V, the CDR exhibits growth over the entire region extending from $\hat{k}=0$ to the FDR downshifted peak, and $\text{Im}(\hat{\omega})$ for the CDR approaches the asymptote $\hat{\omega}_c\hat{\omega}_p = 0.005$ as $\hat{k}$ approaches infinity.

Plots of $\text{Re}(\hat{\omega})$ versus $\hat{k}$ for the CDR and FDR in the downshifted growth intervals of $\hat{k}$ are shown in Fig. 11(a). Note that both the FDR and CDR exhibit positive and negative group velocities over the interval of the downshifted peak. We also note that below $\hat{k}\approx 0.5$, the real frequency $\text{Re}(\hat{\omega})$ for the CDR exceeds $\hat{k}\beta_b$, in agreement with Eq. (58), which gives the solution for $\hat{\omega}$ that solves the CDR for small values of $\hat{k}$.

Figure 11(b) shows plots of $\text{Re}(\hat{\omega})$ versus $\hat{k}$ for the CDR and FDR in the upshifted growth regions. It follows that $\text{Re}(\hat{\omega}) < \hat{k}\beta_b$ for both the CDR and FDR in these regions. However, the difference between $\hat{k}\beta_b$ and $\text{Re}(\hat{\omega})$ (for both the FDR and CDR) becomes very small as $\hat{k}$ increases from its value at the FDR peak towards the upper boundary of the FDR growth curve. The above behavior for the FDR conforms with the discussion in Sec. III. Consider Fig. 1(b) in circumstances where the LHS parabola shifts to the left (with increasing $\hat{k}$) in order to relink with the RHS curve in the interval $0 < \hat{\omega} < \hat{\omega}_-$. The minimum of the LHS parabola lies below $\hat{\omega} = \hat{k}\beta_b$. If the slope of the RHS curve below this minimum is approximately zero, then the parabola minimum can approach close to the RHS curve at values of $\hat{k}$ which are much smaller than $\hat{k} \simeq \hat{k}_{ub}$, where the relinking finally takes place. At such values of $\hat{k}$ we have $\mathrm{Re}(\hat{\omega}) \simeq \hat{k}\beta_b$. These values of $\hat{k}$ constitute the tail region which follows the FDR upshifted maximum in Fig. 10(b).

In Fig. 12, we plot the frequency mismatches for this system as functions of $\hat{k}$, over the interval of the FDR upshifted peak. Consider the plot of the mismatch $|\hat{\omega}-\hat{k}\beta_b|$ versus $\hat{k}$. A validity condition [Eq. (34)] for the CDR is $|\hat{\omega}-\hat{k}\beta_b| >> \hat{\omega}_p/\gamma_b$. For values of $\hat{k}$ at the onset and maximum of the FDR growth curve, $|\hat{\omega}-\hat{k}\beta_b|$ is about four times $\hat{\omega}_p/\gamma_b$. However, $|\hat{\omega}-\hat{k}\beta_b|$ decreases very rapidly with increasing $\hat{k}$, and the CDR is not valid over most of the FDR growth region. The behavior in Fig. 12 conforms closely to the relative behavior of the FDR and CDR growth curves shown in Fig. 10(b). Further properties of Fig. 12 will be considered in Sec. IX.

B. Example 2 (γ_0=2.0, $\hat{\omega}_p$=$\sqrt{0.4}$, $\hat{\omega}_c$=0.5) - Raman System

We increase the value $\hat{\omega}_p$ of Example 1 from 0.01 to $\sqrt{0.4}$ to obtain a system with parameters γ_0=2.0, $\hat{\omega}_p$=0.6324... and $\hat{\omega}_c$=0.5. This system is located at the point $1/\gamma_b^2 = 0.5$ and $\hat{\omega}_c^2/\hat{\omega}_p = 0.395$ in Fig. 9(b). Figure 13 shows both the CDR and FDR growth rate curves $\mathrm{Im}(\hat{\omega})$ versus $\hat{k}$, for this system. The classification of the system is clearly Raman according to the terminology in Secs. VI and VII. The downshifted and upshifted peaks are combined into a single peak, and the upper and lower bounds on the gap [$\hat{k}'_{ub}$ and $\hat{k}'_{\ell b}$ of Eq. (49)] do not appear since the sufficiency condition $\hat{\omega}_p \gtrsim \gamma_b\beta_b/2$ [Eq. (50)] for no gap is also satisfied. [It follows that the equation $\hat{\omega}_\ell(\hat{k})$=$\hat{\omega}_-(\hat{k})$ cannot be satisfied for this system.] We see that $\hat{k}_{\ell b}$ and $\hat{k}_{ub}$ [Eq. (48)] provide a useful estimate of the $\hat{k}$-

interval for which there is growth, but not a good approximation for its boundaries.

Figure 14 shows a plot of $\mathrm{Re}(\hat{\omega})$ versus $\hat{k}$ in the FDR and CDR growth intervals. Near $\hat{k}=0$, $\mathrm{Re}(\hat{\omega})>\hat{k}\beta_b$ for the CDR. Both the CDR and FDR solutions approach the curve $\hat{\omega}=\hat{k}\beta_b$ as $\hat{k}$ increases, but do not approach it rapidly, as they do in the Compton Example 1. Neither the CDR nor FDR curves show a region of negative group velocity below $\hat{k}=1$, as they do in Example 1 [Fig. 11(b)].

Frequency mismatches for the FDR are shown in Fig. 15. Clearly the CDR validity condition, $|\hat{\omega}-\hat{k}\beta_b| >> \hat{\omega}_p/\gamma_b$, is satisfied nowhere within the interval of the FDR growth curve. The strong inequality in Eq. (71), for the validity of the approximation in Eq. (69) to the Raman dispersion relation (68), is satisfied marginally by this system [with $0.534 << 1.79$]. For $\hat{k}=1.8$ (approximately the FDR peak maximum), the mismatches are $|\hat{\omega}-\hat{\omega}_\ell| \simeq |\hat{\omega}-\hat{\omega}_-| \simeq 0.36|\hat{\omega}-\hat{\omega}_u|$. Thus, the assumptions in the Raman approximation [Eq. (68)] to the dispersion relation are marginally satisfied. However, at the right boundary of the FDR peak, $|\hat{\omega}-\hat{\omega}_u| \simeq |\hat{\omega}-\hat{\omega}_-|$, and the assumptions of the derivation are clearly invalid. This behavior is reflected in the accuracy of the Raman approximation (RA) growth rate curve [Eq. (68)] shown in Fig. 13. The RA gives a marginally accurate estimate of the FDR maximum growth rate (an error of 13%), but the detailed RA growth curve is not a good approximation to the FDR growth curve at larger values of $\hat{k}$.

C. Example 3 ($\gamma_0=10$, $\hat{\omega}_p=1.0$, $\hat{\omega}_c=0.03$) - Raman System

An example of a Raman system at relatively high γ_b is given by the choice of parameters $\gamma_0=10$, $\hat{\omega}_p=1.0$, and $\hat{\omega}_c=0.03$. Apart from the cold-beam approximation, these parameters are similar to those given for an Astron beam by Kwan et al.[6] This system is located at the point $1/\gamma_b^2=0.0109$ and $\hat{\omega}_c^2/\hat{\omega}_p=0.0009$ in

Figs. 9(a) and 9(b). Figure 16 shows both the FDR and CDR growth rate curves in the neighborhood of the upshifted peak. (The downshifted peak is not shown.) As is typical for Raman systems, the upper bound $\hat{k}_{ub}$ on the growth region provides a useful (but approximate) estimate of the upper boundary of the unstable $\hat{k}$-range. Moreover, $\hat{k}'_{ub}$ provides a good approximation to the location of the maximum growth rate. Plots of Re($\hat{\omega}$) versus $\hat{k}$ in the upshifted growth region are not included. For the scales of $\hat{k}$ and Re($\hat{\omega}$) involved, such plots are indistinguishable from Re($\hat{\omega}$)=$\hat{k}\beta_b$.

Frequency mismatches are shown in Fig. 17, where $\hat{\omega}$ is computed from the FDR in Eq. (28). As expected, the validity condition $|\hat{\omega}-\hat{k}\beta_b| >> \hat{\omega}_p/\gamma_b$ for the CDR is not satisfied in the interval of the upshifted peak. This system obeys the strong inequality in Eq. (71) (with $0.093 << 0.42$), and the Raman approximation in Eq. (68) is a good approximation to the dispersion relation. In contrast with Example 2, the assumptions in the Raman approximation are satisfied (at least marginally) over the entire interval of the FDR growth curve [with $|\hat{\omega}-\hat{\omega}_\ell| \simeq |\hat{\omega}-\hat{\omega}_-| \simeq 0.21|\hat{\omega}-\hat{\omega}_u|$ at the peak maximum and $|\hat{\omega}-\hat{\omega}_-| \simeq 0.35|\hat{\omega}-\hat{\omega}_u|$ at upper boundary]. The RA growth curve in Fig. 16 is seen to provide a good approximation to that of the FDR, except for a small shift to the left.

IX. PROPERTIES OF THE TAIL REGION

A. Coupled Longitudinal Oscillations

The FDR growth rate curve in Example 1 of the previous section shows a tail extending from the upshifted growth rate maximum [Fig. 10(b)] in the direction of increasing $\hat{k}$. Our numerical analysis has shown that such a tail occurs for all systems classified as Compton or marginally Compton according to the criteria developed in Sec. VI. The underlying reason for such a tail can be seen by analyzing the plots of frequency mismatches versus $\hat{k}$ [e.g., in Fig. 12].

Consider the numerical results in Fig. 12, which shows the frequency mismatches for Example 1 ($\gamma_0=2.0$, $\hat{\omega}_p=0.01$, $\hat{\omega}_c=0.5$) in Sec. VII (a Compton system). Three of the mismatches illustrated in Fig. 12 are $|\hat{\omega}-\hat{\omega}_-|$, $|\hat{\omega}-\hat{\omega}_\ell|$ and $|\hat{\omega}-\hat{\omega}_u|$, where $\hat{\omega}_-(\hat{k}) = [(\hat{k}-1)^2 + \hat{\omega}_p^2]^{1/2}$ is the frequency of the left-hand circularly-polarized radiation field, $\hat{\omega}_\ell(\hat{k}) = \hat{k}\beta_b - \hat{\omega}_p/\gamma_b$ is the frequency of the negative-energy longitudinal oscillation, and $\hat{\omega}_u(\hat{k}) = \hat{k}\beta_b + \hat{\omega}_p/\gamma_b$ is the frequency of the positive energy longitudinal oscillation. At the maximum of the FDR growth curve ($\hat{k}\simeq3.4$), the differences in the values of these three mismatches are small. However, with increasing $\hat{k}$, the mismatch $|\hat{\omega}-\hat{\omega}_-|$ grows in magnitude while $|\hat{\omega}-\hat{\omega}_\ell|$ and $|\hat{\omega}-\hat{\omega}_u|$ decrease toward the value $\hat{\omega}_p/\gamma_b$ (as a result of the mismatch $|\hat{\omega}-\hat{k}\beta_b|$ becoming very small). Thus, in the tail region, $|\hat{\omega}-\hat{\omega}_-|$ becomes almost two orders of magnitude larger than $|\hat{\omega}-\hat{\omega}_\ell|$ and $|\hat{\omega}-\hat{\omega}_u|$. The mismatch $|\hat{\omega}-\hat{\omega}_+|$, not shown in Fig. 12, is approximately 2.0, which is much greater than the mismatches shown in Fig. 12.

The above behavior of the frequency mismatches indicates that the tail in the growth rate curve is produced by a coupling of the two longitudinal modes by the wiggler field and the radiation fields. Although the uncoupled dispersion relations for these modes do not have a common $\hat{\omega}(\hat{k})$, the frequencies in the tail region are very close to the natural frequencies of both longitudinal oscillations.

If the tails are due to such a coupling, an approximate dispersion relation, valid in the tail region can be derived as follows. We express the FDR [Eq. (28)] in the approximate form

$$(\hat{\omega}-\hat{\omega}_\ell)(\hat{\omega}-\hat{\omega}_u) = \mathrm{RHS}(\hat{\omega}=\hat{k}\beta_b,\hat{k}) \ , \tag{72}$$

where $\mathrm{RHS}(\hat{\omega},\hat{k})$ is defined below Eq. (38) and $\hat{\omega}$ in the expression for RHS is replaced by $\hat{k}\beta_b$. We refer to Eq. (72) as the longitudinal-longitudinal (LL) approximation to the FDR. From it we obtain the following analytic expression for the growth rate

$$\mathrm{Im}(\hat{\omega}) = \hat{\omega}_p\left\{\frac{\hat{\omega}_c^2(1+\hat{\omega}_p^2+\hat{k}^2/\gamma_b^2)(\hat{\omega}_p^2+\hat{k}^2/\gamma_b^2)}{(2\hat{k}+1+\hat{\omega}_p^2+\hat{k}^2/\gamma_b^2)(-2\hat{k}+1+\hat{\omega}_p^2+\hat{k}^2/\gamma_b^2)} - \frac{1}{\gamma_b^2}\right\}^{1/2} , \tag{73}$$

or $\mathrm{Im}(\hat{\omega})=0$, if the right-hand side of Eq. (73) is pure imaginary. The quantity $\mathrm{Im}(\hat{\omega})$ approaches infinity as $\hat{k}$ approaches $\hat{k}_{LL1}$ from below or $\hat{k}_{LL2}$ from above, where

$$\left.\begin{matrix}\hat{k}_{LL1}\\ \hat{k}_{LL2}\end{matrix}\right\} = \gamma_b^2\left\{1 \mp [1-(1+\hat{\omega}_p^2)/\gamma_b^2]^{1/2}\right\} . \tag{74}$$

A plot of $\mathrm{Im}(\hat{\omega})$ versus $\hat{k}$ for the LL approximation [Eq. (73)] is included in Fig. 10(b) for Example 1. In Fig. 17, we show the FDR upshifted peak and the LL approximation for a system with $\gamma_0=50$, $\hat{\omega}_p=0.006$ and $\hat{\omega}_c=0.015$.[8] From Figs. 10(b) and 18, the LL approximation provides an excellent approximation in the tail regions of both systems.

In Sec. II, we derived Eqs. (35) - (37) for the field energy ratios E_L/E_-, E_L/E_+ and E_+/E_-. Here, E_L, E_-, and E_+ are, respectively, the energy densities of the longitudinal waves and the left- and right-hand circularly-polarized radiation fields. We consider the behavior of these ratios as $\hat{k}$ varies from the region of maximum growth to the tail region. Plots of these ratios as functions of $\hat{k}$, over the interval of the upshifted growth region, are shown in Fig. 19 for the parameters used in Example 1 of Sec. VIII.

We note that most of the energy resides in the left-hand circularly-polarized radiation field. However, as $\hat{k}$ increases from the left boundary of the upshifted growth curve to the edge of the tail region in Fig. 10(b), the ratio E_L/E_- increases over two orders-of-magnitude from the (very small) value $E_L/E_- \simeq 3.6 \times 10^{-4}$ to the (small) value $E_L/E_- \simeq 1.4 \times 10^{-1}$.

An estimate of the ratio E_L/E_- at the edge of the tail region is obtained by setting $\hat{\omega}=\hat{k}\beta_b$, in Eq. (36). We obtain

$$\left(\frac{E_L}{E_-}\right)_{\hat{\omega}=\hat{k}\beta_b} = \hat{\omega}_c^2 \frac{2}{(1+\beta_b^2+2/\hat{k}+1/\hat{k}^2)} \frac{(\hat{k}^2\beta_b^2-\hat{\omega}_2^2)}{(\hat{k}^2\beta_b^2-\hat{\omega}_+^2)} . \tag{75}$$

The factor 2/(...) in Eq. (75) is of order unity since $\hat{k}>1$ at the edge of the tail region. Referring to Fig. 1(b), and noting that $\hat{k}\beta_b$ is to the left of $\hat{\omega}_-$ at the edge of the tail region, we find that the final ratio in Eq. (75) is also of order unity. We therefore conclude that

E_L/E_- is of order $\hat{\omega}_c^2$ at the edge of the tail region and consequently can be quite small. For a high-gamma system such as that in Fig. 18, Eq. (75) simplifies to give

$$\left(\frac{E_L}{E_-}\right)_{\hat{\omega}=\hat{k}\beta_b} \simeq \frac{2\hat{\omega}_c^2}{(1+\beta_b^2)} \frac{\gamma_0^2}{(\gamma_0+\gamma_b)^2} \simeq \hat{\omega}_c^2 \frac{\gamma_0^2}{(\gamma_0+\gamma_b)^2} . \tag{76}$$

We conclude that although the detailed structure of the tail region is associated with coupled longitudinal oscillations, the major portion of the field energy associated with this region resides in the radiation field. However, the ratio E_L/E_- can be expected to increase significantly as $\hat{k}$ varies from the left side of the upshifted peak to the edge of the tail region.

B. Conditions for Existence of a Tail Region for Large-Gamma Systems

Two conditions are required for a tail region to exist as in Fig. 10(b). First, for an interval $\hat{k}$ within the growth region, it is necessary that

$$|\hat{\omega}-\hat{k}\beta_b| << \hat{\omega}_p/\gamma_b , \tag{77}$$

in order that $|\hat{\omega}-\hat{\omega}_\ell|$ and $|\hat{\omega}-\hat{\omega}_u|$ have approximately the same value. Second, it is required that

$$|\hat{\omega}-\hat{\omega}_u| << |\hat{\omega}-\hat{\omega}_-| , \tag{78}$$

in order that the coupling is primarily between the longitudinal modes. Note that the inequalities in Eqs. (34) and (77) are not contradictory, since they apply to different $\hat{k}$-regions of the upshifted FDR growth curve.

Recalling the discussion in Sec. III, and considering Fig. 1(b) for the case where $\hat{k}$ corresponds to the upper boundary of the upshifted peak, it follows that the LHS parabola, shifting to the left, is tangent to the RHS curve for $0 < \hat{\omega} < \hat{\omega}_-$. The double real root $\hat{\omega}$ of the FDR corresponding to this tangency is the frequency at the upper boundary of the growth curve. To satisfy the condition in Eq. (77), we require that the magnitude of the common slope of the LHS and RHS curves at the point of tangency be much less than $2\hat{\omega}_p/\gamma_b$, since the magnitude of the slope of the parabola is $2|\hat{\omega}-\hat{k}\beta_b|$. If we approximate the slope of the RHS curve at this tangency by the value at $\hat{k}_{ub}$ [the upper bound on the growth region defined in Eq. (48)], then the condition in Eq. (77) is replaced by

$$\left|\frac{\partial}{\partial\hat{\omega}}\,\mathrm{RHS}(\hat{\omega},\hat{k}_{ub})\right|_{\hat{\omega}=\hat{k}_{ub}\beta_b} << \frac{2\hat{\omega}_p}{\gamma_b}\ . \tag{79}$$

If Eq. (79) holds (assuring a small slope), then Eq. (78) can be approximated by substituting $\hat{k}=\hat{k}_{ub}$ and $\hat{\omega}=\hat{k}_{ub}\beta_b$, which gives

$$\frac{\hat{\omega}_p/\gamma_b}{|\hat{\omega}_-(\hat{k}_{ub})-\hat{k}_{ub}\beta_b|} << 1\ . \tag{80}$$

It is not difficult to apply the inequalities in Eqs. (79) and (80) to most high-gamma systems. We differentiate RHS, using Eq. (38). For systems satisfying

$$2\gamma_b^2 >> 1 + \hat{\omega}_p^2\ , \tag{81}$$

the inequality in Eq. (79) then reduces to

$$\frac{16\gamma_0\gamma_b^2(\gamma_0-\gamma_b)\hat{\omega}_p}{(\gamma_0+\gamma_b)[4\gamma_0(\gamma_0-\gamma_b)+1+\hat{\omega}_p^2]^2} << 1 . \qquad (82)$$

Making use of Eqs. (81), (42), and (48), the inequality in Eq. (80) becomes

$$\hat{\omega}_p << \gamma_0 . \qquad (83)$$

Since large-gamma systems are assumed, Eq. (83) is similar to Eq. (81). In addition, it is assumed that

$$4\gamma_0(\gamma_0-\gamma_b) >> 1 + \hat{\omega}_p^2 . \qquad (84)$$

This condition would be violated by a high-gamma system only for extremely low wiggler field [Eq. (32)]. If the inequality in Eq. (84) holds, then with the aid of Eq. (32) we simplify the inequality in Eq. (82) to give

$$\frac{\hat{\omega}_p}{\gamma_0^3\hat{\omega}_c^2} << 1 , \qquad (85)$$

as the condition for the existence of a tail region in a high-gamma system.

Consider the condition in Eq. (62) for the validity of the Compton approximation at the maximum of the upshifted growth curve. For high-gamma systems, $\beta_b \approx 1$ and $\hat{k} \approx 2\gamma_b^2$ at this maximum. Then the inequality in Eq. (62) reduces to

$$\frac{2\hat{\omega}_p}{\gamma_b^3\hat{\omega}_c^2} << 1 . \qquad (86)$$

Comparing Eqs. (85) and (86), we conclude that all cold-beam high-gamma

Compton systems have a tail region produced by coupled longitudinal oscillations.

X. CONCLUSIONS

In this paper, we have given rigorous derivations of properties of the cold-fluid full dispersion relation (FDR) in Eq. (28). Such properties include the upper and lower bounds on the unstable growth region in $\hat{k}$-space as given by Eq. (48), and on the gap between the downshifted and upshifted peaks as given by Eqs. (50). From these bounds, we have derived sufficient conditions that a cold beam be stable for all values of $\hat{k}$ and that the downshifted and upshifted peaks merge together. We have also verified that the cold-fluid FDR [Eq. (28)] as well as the cold-fluid CDR [Eq. (33)] have at most one unstable branch with $\mathrm{Im}(\hat{\omega}) > 0$ for any value of $\hat{k}$.

The full Compton dispersion relation (CDR) in Eq. (33) has been derived by making the single additional assumption that the electrostatic perturbations may be neglected ($\delta\phi \simeq 0$). We have shown that the detailed growth curves obtained from the cold-fluid CDR differ substantially from those obtained from the cold-fluid FDR except possibly at maximum growth and in the region between the growth peaks. Equation (64) is the (numerically-deduced) condition for the Compton approximation to be valid to within 10% at the maximum growth rate of the upshifted peak for cold-beam systems.

Results of detailed numerical analysis of the dispersion relations are presented in Sec. VIII. This analysis shows that the relative values of frequency mismatches may vary significantly over the interval of the upshifted FDR peak. Thus, approximations which adequately predict the maximum growth rate do not necessarily give an adequate description of the detailed shape of the peak. As $\hat{k}$ increases over the region of the upshifted peak, $|\hat{\omega}-\hat{\omega}_-|$ increases and $|\hat{\omega}-\hat{k}\beta_b|$ decreases. The decrease of the latter causes both $|\hat{\omega}-\hat{\omega}_\ell|$ and $|\hat{\omega}-\hat{\omega}_u|$ to approach the value $\hat{\omega}_p/\gamma_b$. For Compton systems, the result is a change in the appropriate approximation to the FDR [Eq. (28)] from the CDR [Eq. (33)] in the maximum growth region, to the LL-approximation [Eq. (73)] for $\hat{k}$ in the tail region. The Raman approximation [Eq. (68)] also becomes invalid if $|\hat{\omega}-\hat{\omega}_-|$ and $|\hat{\omega}-\hat{\omega}_u|$ are approximately equal before the growth rate has decreased to zero with increasing $\hat{k}$.

An interesting property of the upshifted FDR growth curves for Compton systems is the tail which extends from maximum growth in the direction of increasing $\hat{k}$. In Sec. IX, we showed that the mechanism producing this tail is associated with a coupling of the positive- and negative-energy longitudinal oscillations by the wiggler and radiation fields. In most cases, the dominant field energy associated with this instability is concentrated in the radiation field.

We conclude with some important remarks concerning thermal effects. The above result that the CDR [Eq. (33)] can never adequately approximate the detailed shape of the FDR growth curves [Eq. (28)] holds in the cold-fluid approximation. It is not a general result applicable to systems with finite temperature described by either Vlasov or warm-fluid versions of the FDR or CDR. We also note that the tail regions for Compton systems decrease in size when finite-temperature effects are included. The important influence of thermal effects will be presented in a subsequent paper.

ACKNOWLEDGMENTS

This research was supported in part by the Office of Naval Research and in part by the National Science Foundation.

REFERENCES

1. R. C. Davidson and H. S. Uhm, Phys. Fluids 23, 2076 (1980).
2. The approach used in this section and in Sec. V is suggested by an analysis by I. B. Bernstein and J. L. Hirshfield in Phys. Rev. A 20, 1661 (1979).
3. J. R. Carey and T. Kwan, Phys. Fluids 24, 729 (1981).
4. N. M. Kroll and W. A. McMullin, Phys. Rev. A 17, 300 (1978).
5. W. A. McMullin, Ph.D. Thesis, University of California, San Diego (1980).
6. T. Kwan, J. M. Dawson, and A. T. Lin, Phys. Fluids 20, 581 (1977).
7. T. Kwan, Ph.D. Thesis, University of California, Los Angeles (1978), p. 59.
8. L. R. Elias, W. M. Fairbank, J. M. Madey, H. A. Schwettman, and T. I. Smith, Phys. Rev. Lett. 36, 717 (1976).

APPENDIX A: VALIDITY OF THE COMPTON APPROXIMATION

In deriving the criterion presented in Eq. (64) and Fig. 9 for validity of the Compton approximation, we have solved numerically the full dispersion relation (28) and the Compton dispersion relation (33) in the region of maximum growth for the upshifted peak for a wide range of system parameters. Detailed comparisons of growth rate and real frequency have been made for system parameters covering more than seventy-five points in the parameter space (x,y), where

$$x = \frac{1}{\gamma_b^2} = \frac{1}{\gamma_0^2} + \hat{\omega}_c^2 \, ,$$

$$y = \frac{\hat{\omega}_c^2}{\hat{\omega}_p} \, . \tag{A.1}$$

Rather than tabulating here these extensive numerical results, we summarize stability properties for several points (x^*,y^*) located exactly on the curve

$$y^* = 25\sqrt{x^*}\,\sqrt{1-x^*}\,(1 - \sqrt{1-x^*}) \, . \tag{A.2}$$

Table I shows a comparison of numerical results for x^* covering the range from 0.005 to 0.992 and y^* from 0.0044 to 5.530. The values of $\text{Im}\hat{\omega}$, $\text{Re}\hat{\omega}$ and $\hat{k}$ listed in Table I are calculated from the full dispersion relation (28). The corresponding percentage errors in $\text{Im}\hat{\omega}$ and $\text{Re}\hat{\omega}$ incurred by using the Compton dispersion relation (33) are also shown. Table I illustrates that the inequality in Eq. (64) is indeed a good criterion for the Compton dispersion relation (33) to be marginally valid (within 10% error).

Finally, for completeness, Table II shows a similar comparison of stability results from Eqs. (28) and (33) for values of (x,y) just above the dashed curve in Fig. 9, i.e., for (x,y) satisfying

$$y > 70x\sqrt{1-x}\,(1 - \sqrt{1-x}\,). \tag{A.3}$$

It is evident from Table II that the error incurred by using the Compton dispersion relation (33) is indeed less than 5% when the inequality in Eq. (A.3) is satisfied.

Equilibrium Parameters			Equilibrium Parameters		Equation (28)			Equation (33)	
γ_0	$\hat{\omega}_p$	$\hat{\omega}_c$	$x = \frac{1}{\gamma_0^2} + \hat{\omega}_c^2$	$y = \frac{\hat{\omega}_c^2}{\hat{\omega}_p}$	$\mathrm{Im}\hat{\omega}$	$\mathrm{Re}\hat{\omega}$	$\hat{k}$	$\frac{\Delta \mathrm{Im}\hat{\omega}}{\mathrm{Im}\hat{\omega}}$	$\frac{\Delta \mathrm{Re}\hat{\omega}}{\mathrm{Re}\hat{\omega}}$
1.006	0.0020	0.0637	0.9920	2.0279	0.00293	0.0956	1.0968	9.3%	0.7%
1.026	0.0317	0.2164	0.9960	1.4780	0.05710	0.03197	1.005	5.0%	9.8%
1.159	0.0100	0.2352	0.8000	5.5300	0.01313	0.794	1.800	9.6%	0.9%
2.732	0.1000	0.6050	0.5000	3.6603	0.1088	2.287	3.34	10.0%	4.5%
3.993	0.1300	0.3705	0.2000	1.0560	0.0887	8.26	9.3	10.2%	3.4%
5.774	0.1011	0.1000	0.0400	0.0990	0.02988	48.085	491.	9.9%	1.0%
20.000	0.5664	0.0500	0.0050	0.0044	0.0602	393.	394.	10.1%	2.0%

Table I. Comparison of stability properties obtained from FDR [Eq. (28)] and CDR [Eq. (33)] for a range of system parameters (x,y) located on the solid curve $y^* = 25\sqrt{x^*}\,\sqrt{1-x^*}\,\left(1-\sqrt{1-x^*}\right)$ in Fig. 9.

Equilibrium Parameters			Equilibrium Parameters		Equation (28)			Equation (33)	
γ_0	$\hat{\omega}_p$	$\hat{\omega}_c$	$x = \frac{1}{\gamma_0^2} + \hat{\omega}_c^2$	$y = \frac{\hat{\omega}_c^2}{\hat{\omega}_p}$	$\mathrm{Im}\hat{\omega}$	$\mathrm{Re}\hat{\omega}$	$\hat{k}$	$\frac{\Delta \mathrm{Im}\hat{\omega}}{\mathrm{Im}\hat{\omega}}$	$\frac{\Delta \mathrm{Re}\hat{\omega}}{\mathrm{Re}\hat{\omega}}$
1.009	0.0010	0.0894	0.9900	8.0000	0.002342	0.1094	1.1106	4.1%	0.0%
1.200	0.00060	0.1000	0.7044	16.6667	0.001134	1.1902	2.191	4.5%	0.0%
1.504	0.0224	0.5981	0.8000	16.0000	0.04453	0.7739	1.796	4.7%	1.2%
2.000	0.0208	0.5000	0.5000	12.0000	0.03404	2.3829	3.401	4.5%	0.7%
7.071	0.0400	0.5292	0.3000	7.0000	0.05367	5.0797	6.11	4.2%	0.7%
10.000	0.0200	0.0300	0.0109	0.0450	0.004695	181.85	182.85	4.5%	0.1%
10.000	0.0400	0.2000	0.0500	1.0000	0.02733	38.44	39.46	2.7%	0.3%
20.000	0.1250	0.0500	0.0050	0.0200	0.02282	398.0	399.0	3.6%	0.0%
50.000	0.0060	0.0150	0.00063	0.0375	0.001378	3198.4	3199.4	0.3%	0.0%
50.000	0.0100	0.1000	0.0104	1.0000	0.00686	191.0	192.	0.6%	0.0%
50.000	0.1000	0.1000	0.0104	0.1000	0.0317	191.	192.	2.6%	0.0%

Table II. Comparison of stability properties obtained from FDR [Eq. (28)] and CDR [Eq. (33)] for a range of system parameters (x,y) located above the dashed curve $y = 70\sqrt{x}\,\sqrt{1-x}\ \ (1-\sqrt{1-x})$ in Fig. 9.

FIGURE CAPTIONS

Fig. 1 Schematic plots of LHS versus RHS for the FDR [Eqs. (28) and (38)] for $\hat{k}$ in the intervals: (a) $0 < \hat{k} < 1/2$, and (b) $\hat{k} > 1/2$.

Fig. 2 Schematic plot of LHS versus RHS for the FDR [Eqs. (28) and (38)] for $\hat{k}$ in the interval between the upshifted and downshifted peaks.

Fig. 3 Schematic plots of the FDR (solid line) and the CDR (broken line) growth rate curves [Eqs. (28) and (33)] for the cases corresponding to: (a) a single growth rate maximum, and (b) two distinct downshifted and upshifted peaks.

Fig. 4 The region in $(\hat{\omega}_p, \gamma_b)$ space above the curve satisfies the sufficiency condition [Eq. (50)] for overlap of the downshifted and upshifted growth regions in $\hat{k}$-space.

Fig. 5 Plot showing the sufficient condition for the stability of a cold beam [Eq. (53)]. For a specified (γ_b, γ_0), the system is stable for all $\hat{\omega}_p^2$ exceeding $[\hat{\omega}_p^2]_{MIN}$ defined in Eq. (53).

Fig. 6 Plots of growth rate $\mathrm{Im}(\hat{\omega})$ versus $\hat{k}$ obtained numerically from the FDR [Eq. (28)] for several values of $\hat{\omega}_p^2$ and for fixed $\gamma_0=1.3$ and $\gamma_b=1.1$.

Fig. 7 Schematic plots of LHS versus RHS for the CDR [Eqs. (33) and (54)] for $\hat{k}$ in the intervals: (a) $0 < \hat{k} < (1+\hat{\omega}_p)/2$, and (b) $\hat{k} > (1+\hat{\omega}_p)/2$.

Fig. 8 Schematic plot of LHS versus RHS for the CDR [Eqs. (33) and (54)] for values of $\hat{k}$ between the downshifted and upshifted growth rate curves.

Fig. 9 Plot showing the Raman and Compton regions of the parameter space $y=\hat{\omega}_c^2/\hat{\omega}_p$ versus $x=1/\gamma_b^2$ for: (a) large γ_b, and (b) the full range of γ_b. The CDR [Eq. (33)] is valid to within 10% at the (upshifted) growth rate maximum provided $y=\hat{\omega}_c^2/\hat{\omega}_p$ is above the solid curve $y=25\sqrt{x}\sqrt{1-x}(1-\sqrt{1-x})$. The CDR [Eq. (33)] is valid to within 5%

at the upshifted growth rate maximum provided $y=\hat{\omega}_c^2/\hat{\omega}_p$ is above the dashed curve $y=70\sqrt{x}\sqrt{1-x}(1-\sqrt{1-x})$.

Fig. 10 Plots of growth rate Im($\hat{\omega}$) versus $\hat{k}$ for (a) the downshifted peak and (b) the upshifted peak in Example 1. Here $\gamma_0=2$, $\gamma_b^2=2$, $\hat{\omega}_p=0.01$, and $\hat{\omega}_c=0.5$. The FDR and CDR curves refer to Eqs. (28) and (33), respectively.

Fig. 11 Plots of Re($\hat{\omega}$) versus $\hat{k}$ for (a) the downshifted and (b) the upshifted growth regions in Example 1. System parameters are identical to Fig. 10.

Fig. 12 Plots of the frequency mismatches $|\hat{\omega}-\hat{k}\beta_b|$, $|\hat{\omega}-\hat{\omega}_-|$, $|\hat{\omega}-\hat{\omega}_\ell|$ and $|\hat{\omega}-\hat{\omega}_u|$ versus $\hat{k}$ over the interval of the upshifted growth curve in Example 1. Here, parameters are identical to Figs. 10 and 11, and the complex $\hat{\omega}$ solves the FDR in Eq. (28).

Fig. 13 Plots of growth rate Im($\hat{\omega}$) versus $\hat{k}$ for a cold-beam system with $\gamma_0=2$, $\hat{\omega}_p^2=0.4$, $\hat{\omega}_c=0.5$, and $\gamma_b^2=2$. The FDR, CDR, and RA curves refer to Eqs. (28), (33), and (68), respectively. Only a single growth rate maximum is present.

Fig. 14 Plots of Re($\hat{\omega}$) versus $\hat{k}$ for system parameters identical to Fig. 13.

Fig. 15 Plots of the frequency mismatches $|\hat{\omega}-\hat{k}\beta_b|$, $|\hat{\omega}-\hat{\omega}_+|$, $|\hat{\omega}-\hat{\omega}_-|$, $|\hat{\omega}-\hat{\omega}_\ell|$ and $|\hat{\omega}-\hat{\omega}_u|$ versus $\hat{k}$ for system parameters identical to Figs. 13 and 14. Here, the complex $\hat{\omega}$ solves the FDR in Eq. (28).

Fig. 16 Plots of growth rate Im($\hat{\omega}$) versus $\hat{k}$ for the upshifted peak in Example 3. Here, $\gamma_0=10$, $\hat{\omega}_p=1$, $\hat{\omega}_c=0.03$, and $\gamma_b=9.578$. The FDR, CDR, and RA curves refer to Eqs. (28), (33), and (68), respectively.

Fig. 17 Plots of the frequency mismatches $|\hat{\omega}-\hat{k}\beta_b|$, $|\hat{\omega}-\hat{\omega}_+|$, $|\hat{\omega}-\hat{\omega}_-|$, $|\hat{\omega}-\hat{\omega}_\ell|$ and $|\hat{\omega}-\hat{\omega}_u|$ versus $\hat{k}$ for system parameters identical to Fig. 16. Here, the complex $\hat{\omega}$ solves the FDR in Eq. (28).

Fig. 18 Plot of the FDR growth rate $\mathrm{Im}(\hat{\omega})$ versus $\hat{k}$ obtained from Eq. (28) for the upshifted peak, assuming a cold-beam system with parameters $\gamma_0 = 50$, $\hat{\omega}_p = 0.006$, $\hat{\omega}_c = 0.015$, and $\gamma_b = 40$. The LL approximation [Eq. (73)] in the tall region is also shown.

Fig. 19 Plot of the energy ratios E_+/E_-, E_L/E_- and E_L/E_+ versus $\hat{k}$ over the interval of the upshifted peak for Example 1 analyzed in Figs. 10 - 12.

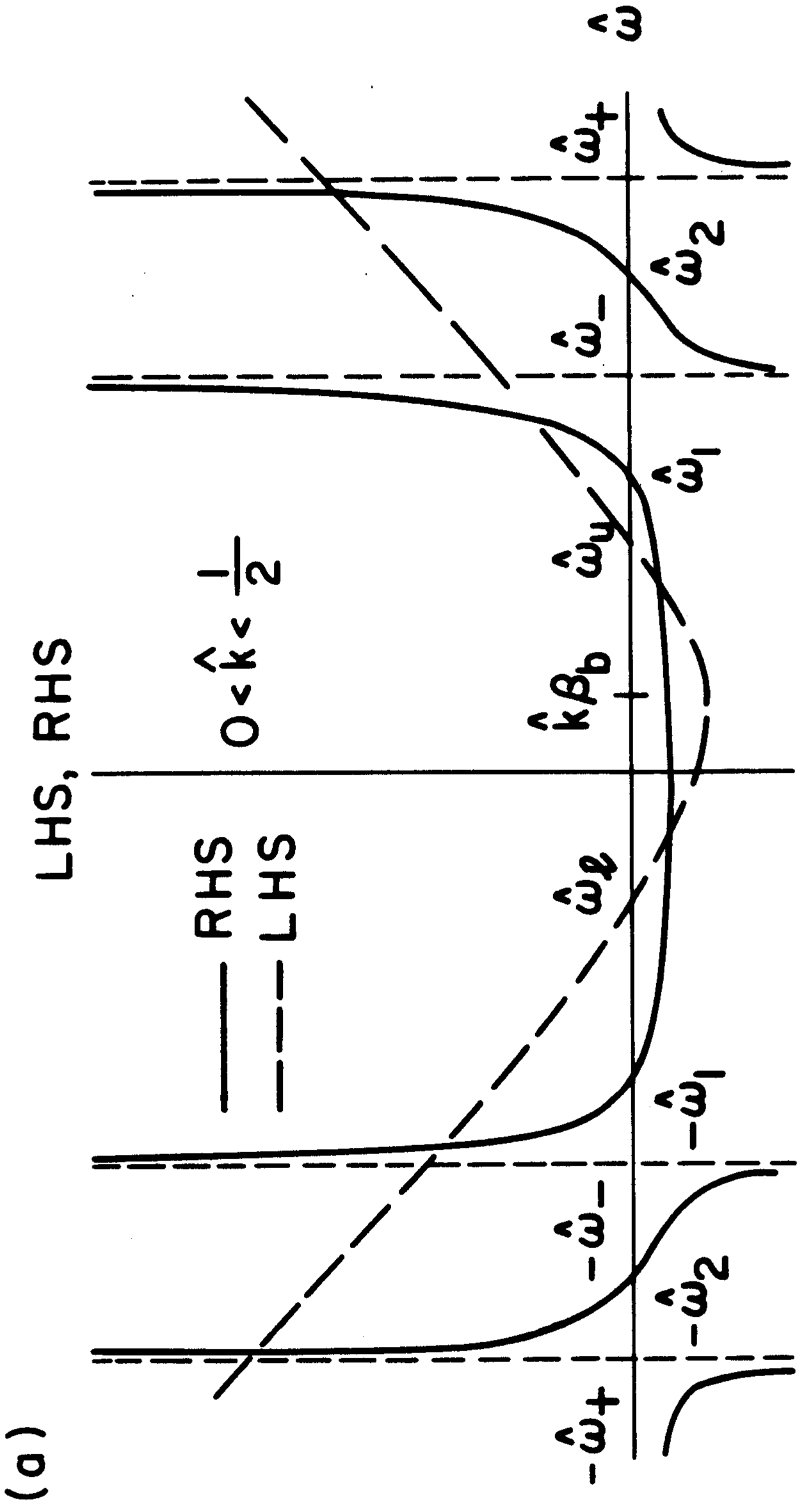
(a)
LHS, RHS
$0<\hat{k}<\frac{1}{2}$
— RHS
– – LHS
$\hat{\omega}$
$\hat{\omega}_+$
$\hat{\omega}_2$
$\hat{\omega}_-$
$\hat{\omega}_1$
$\hat{\omega}_u$
$\hat{k}\beta_b$
$\hat{\omega}_\ell$
$-\hat{\omega}_1$
$-\hat{\omega}_-$
$-\hat{\omega}_2$
$-\hat{\omega}_+$

Fig. 1(a)

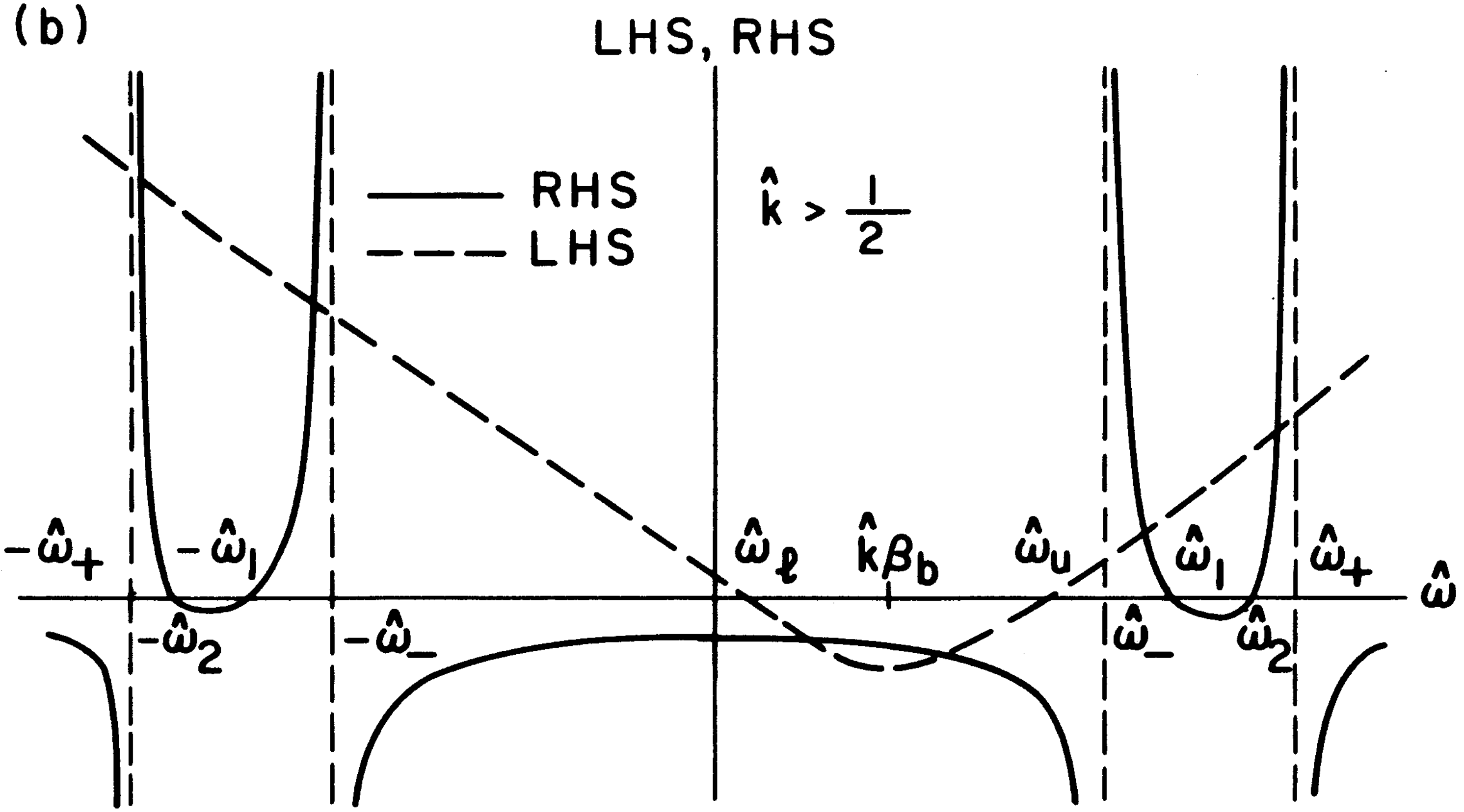
(b)
LHS, RHS
RHS
LHS
$\hat{k} > \frac{1}{2}$
$-\hat{\omega}_+$
$-\hat{\omega}_1$
$-\hat{\omega}_2$
$-\hat{\omega}_-$
$\hat{\omega}_\ell$
$\hat{k}\beta_b$
$\hat{\omega}_u$
$\hat{\omega}_-$
$\hat{\omega}_1$
$\hat{\omega}_2$
$\hat{\omega}_+$
$\hat{\omega}$

Fig. 1(b)

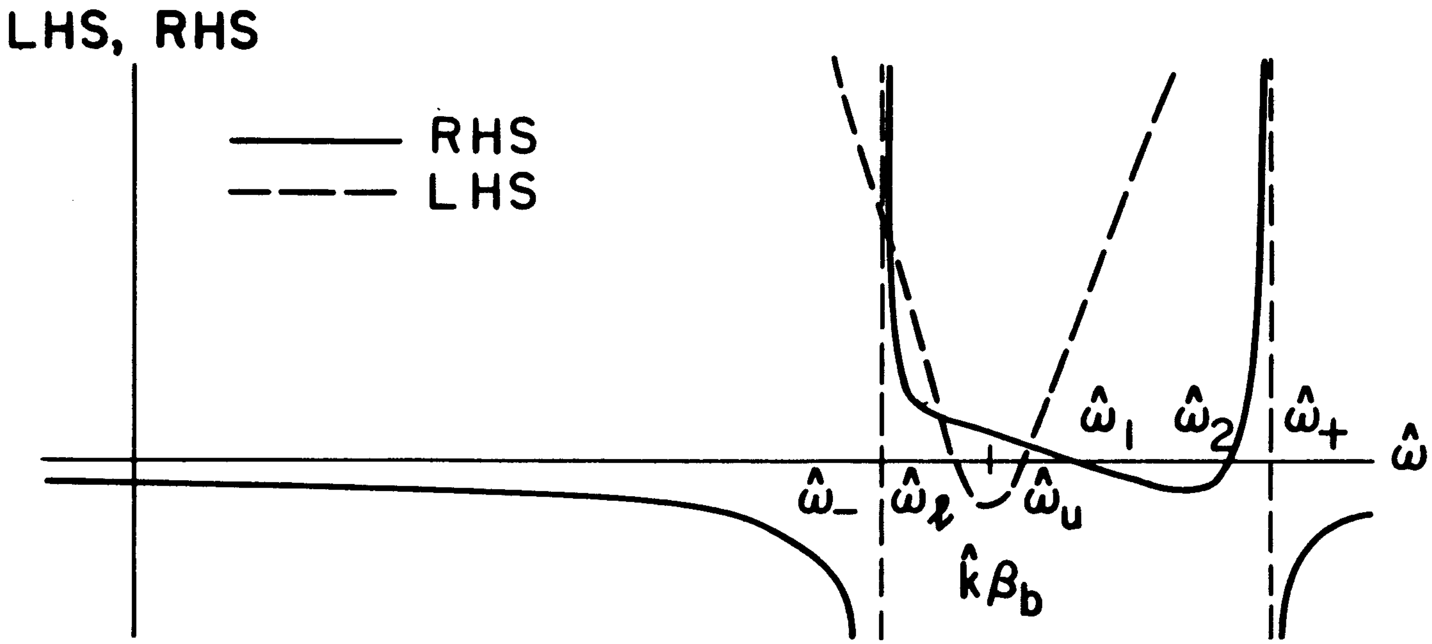
LHS, RHS
RHS
LHS
$\hat{\omega}_-$
$\hat{\omega}_\ell$
$\hat{k}\beta_b$
$\hat{\omega}_u$
$\hat{\omega}_1$
$\hat{\omega}_2$
$\hat{\omega}_+$
$\hat{\omega}$

Fig. 2

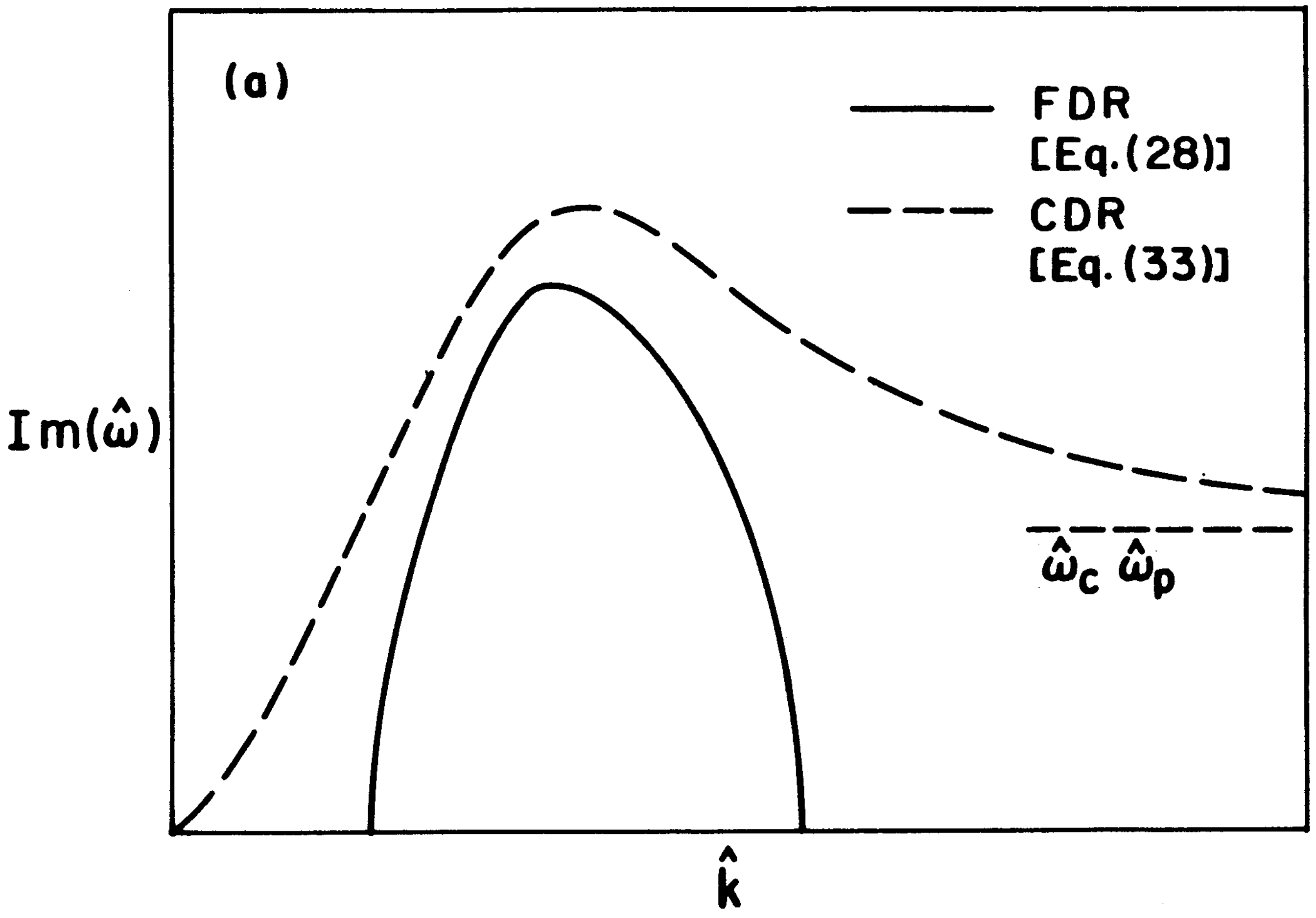
(a)
FDR
[Eq.(28)]
CDR
[Eq.(33)]
$\mathrm{Im}(\hat{\omega})$
$\hat{\omega}_c\ \hat{\omega}_p$
$\hat{k}$

Fig. 3(a)

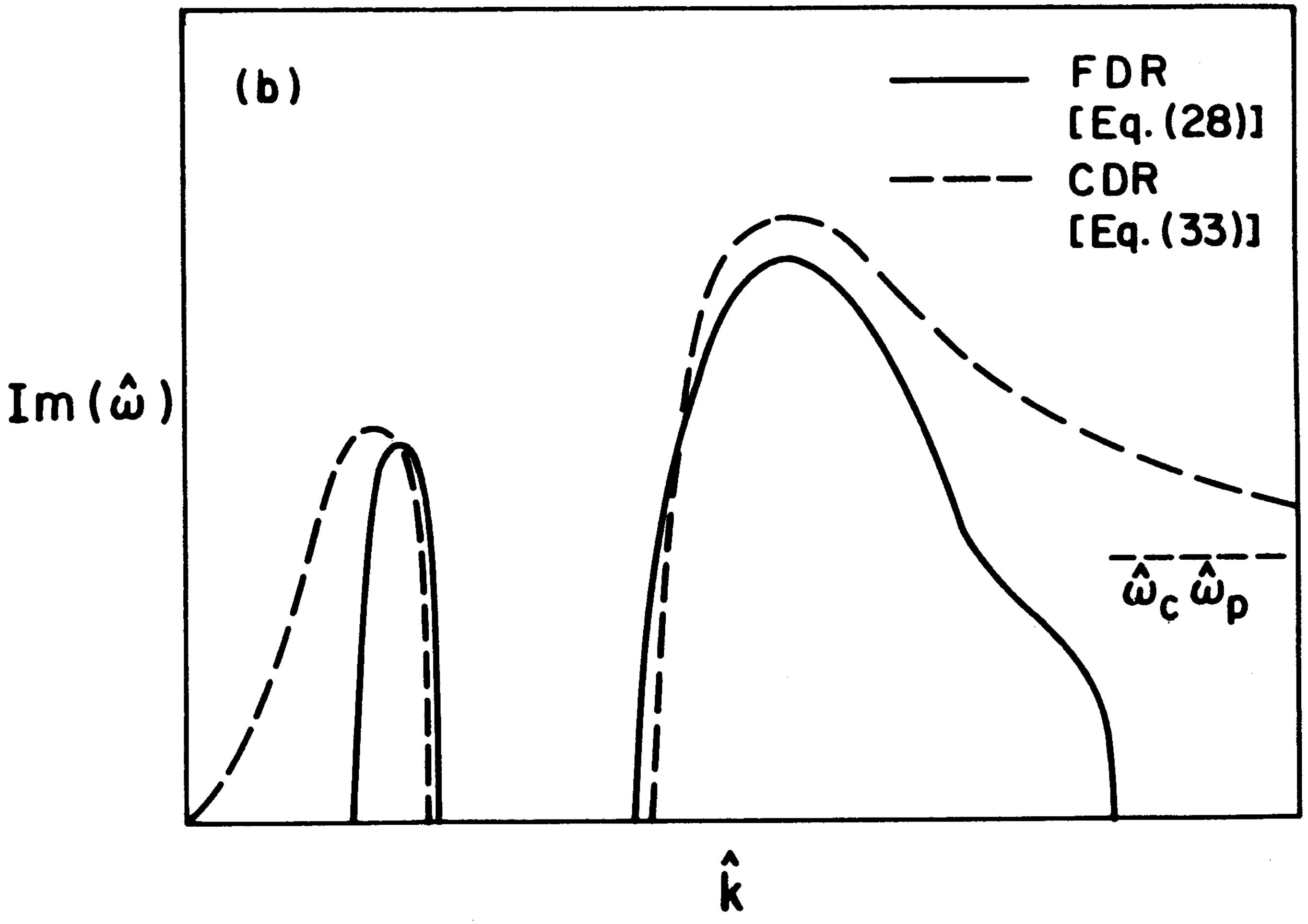
(b)
FDR
[Eq. (28)]
CDR
[Eq. (33)]
$\mathrm{Im}(\hat{\omega})$
$\hat{\omega}_c\hat{\omega}_p$
$\hat{k}$

Fig. 3(b)

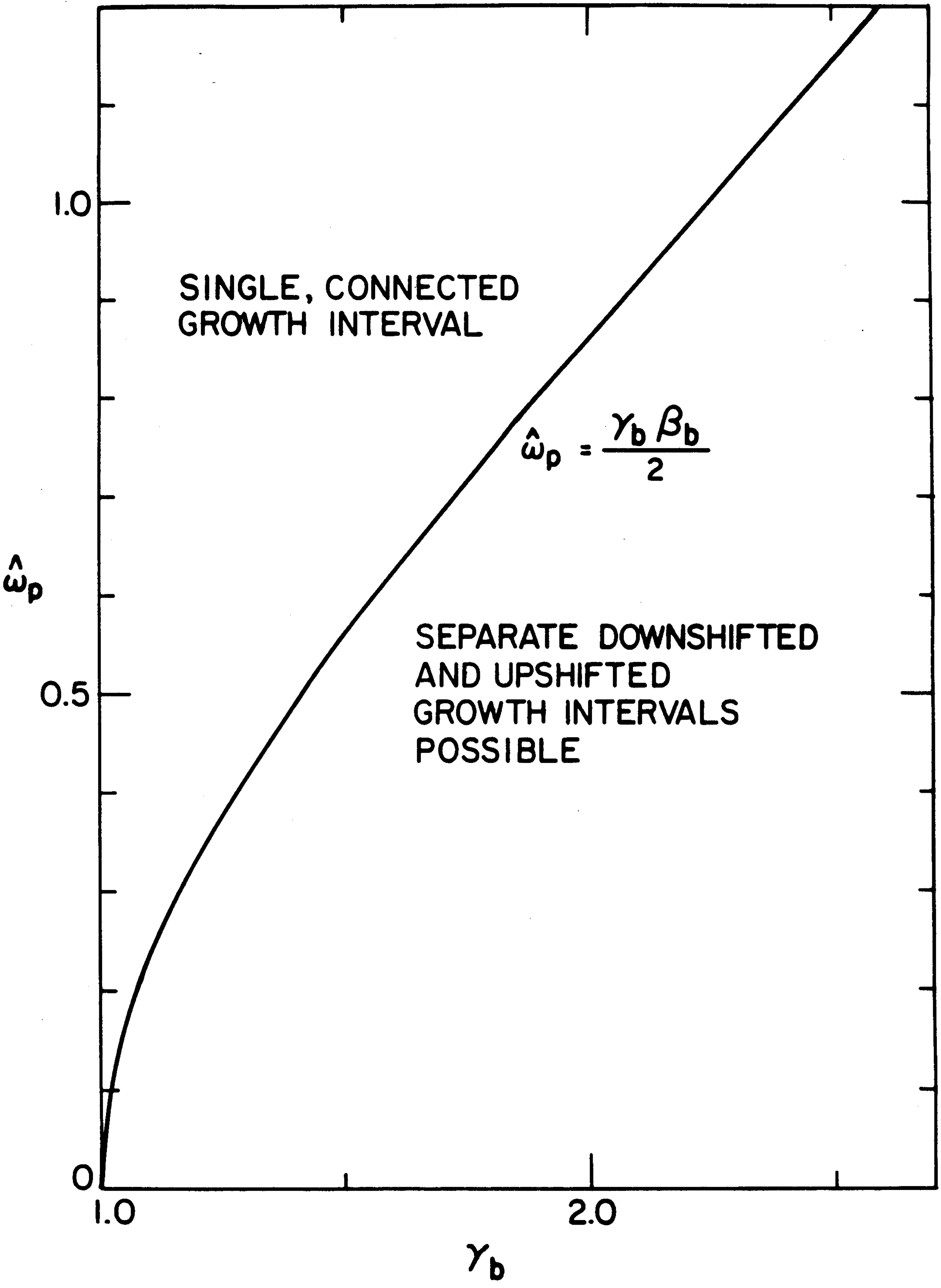
1.0
0.5
0
1.0
2.0
$\hat{\omega}_p$
γ_b
SINGLE, CONNECTED GROWTH INTERVAL
$\hat{\omega}_p = \frac{\gamma_b \beta_b}{2}$
SEPARATE DOWNSHIFTED AND UPSHIFTED GROWTH INTERVALS POSSIBLE

Fig. 4

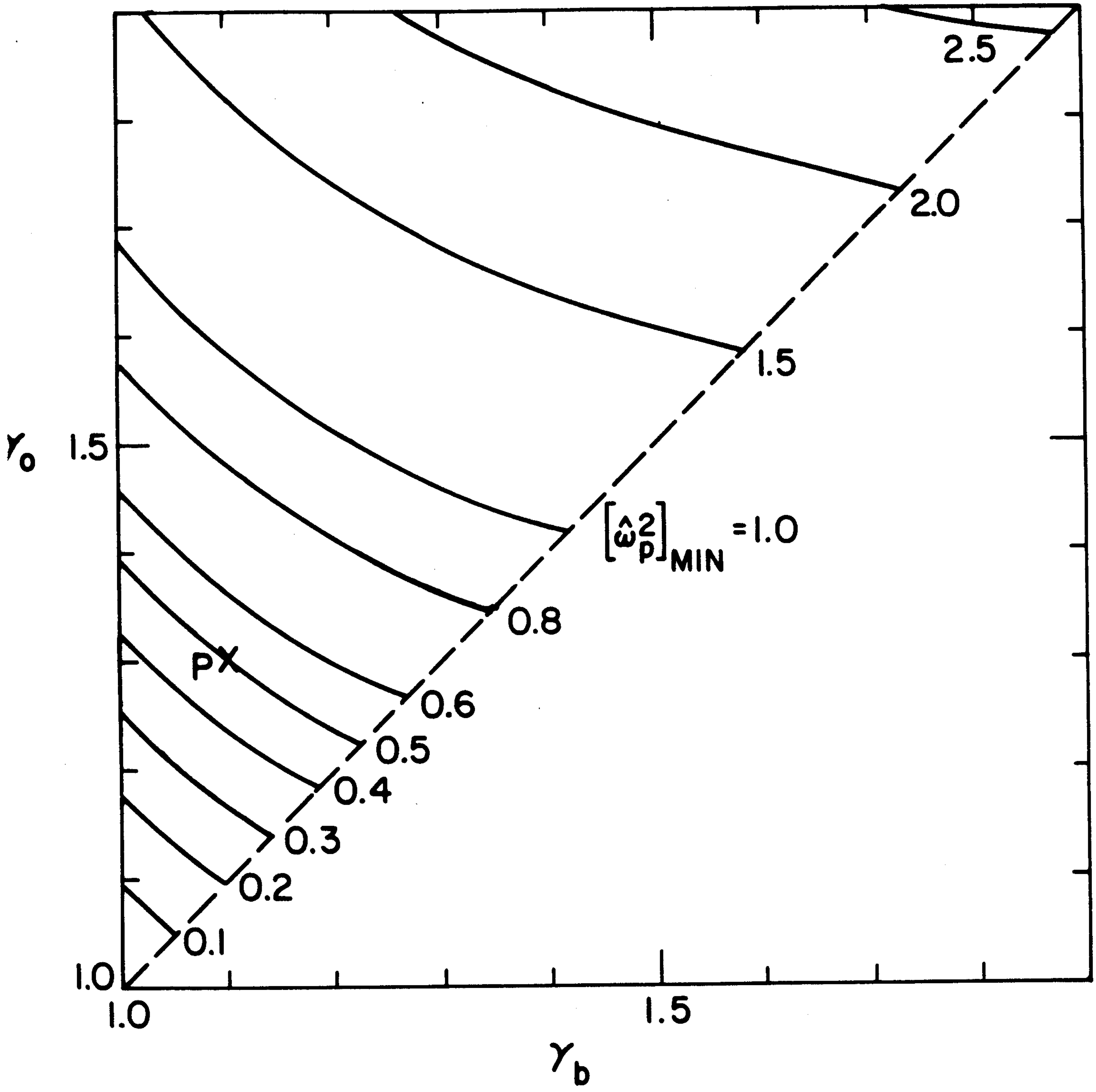
2.5
2.0
1.5
$\left[\hat{\omega}_p^2\right]_{MIN}=1.0$
0.8
0.6
0.5
0.4
0.3
0.2
0.1
P
γ_0
1.5
1.0
1.0
1.5
γ_b

Fig. 5

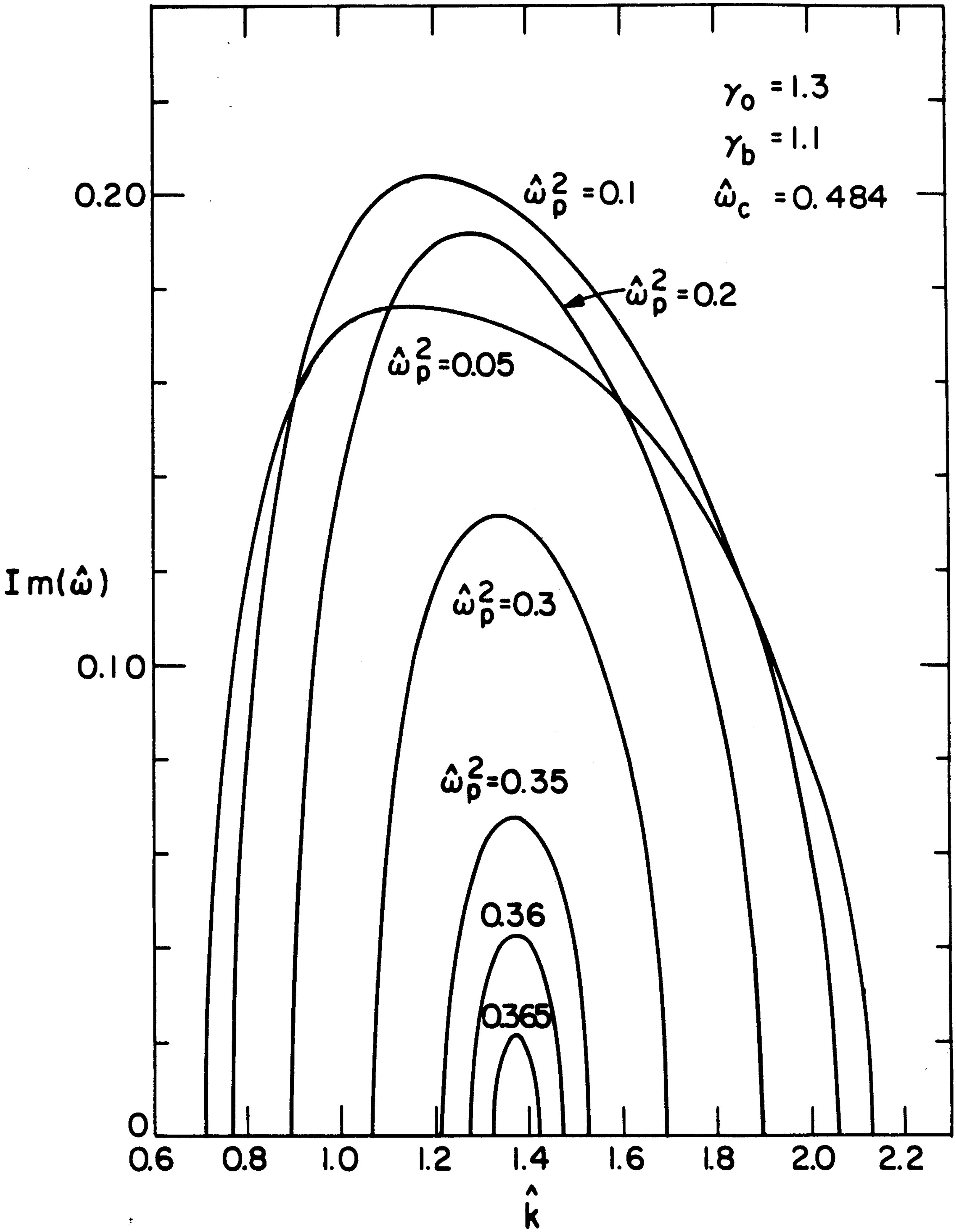
$\gamma_0 = 1.3$
$\gamma_b = 1.1$
$\hat{\omega}_c = 0.484$
$\hat{\omega}_p^2 = 0.1$
$\hat{\omega}_p^2 = 0.2$
$\hat{\omega}_p^2 = 0.05$
$\hat{\omega}_p^2 = 0.3$
$\hat{\omega}_p^2 = 0.35$
0.36
0.365
$\mathrm{Im}(\hat{\omega})$
0.20
0.10
0
0.6
0.8
1.0
1.2
1.4
1.6
1.8
2.0
2.2
$\hat{k}$

Fig. 6

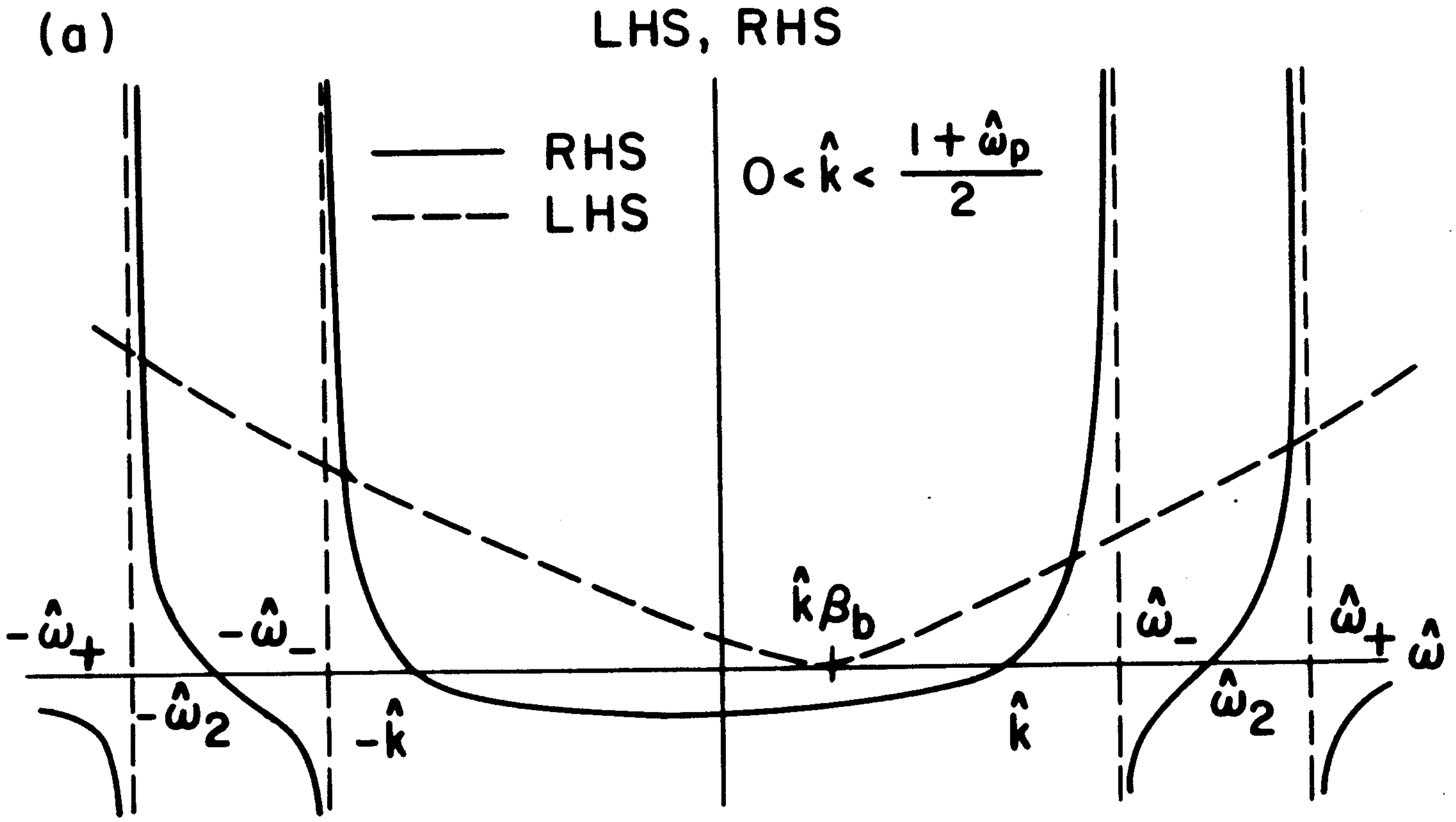
(a)
LHS, RHS
RHS
LHS
$0<\hat{k}<\frac{1+\hat{\omega}_p}{2}$
$-\hat{\omega}_+$
$-\hat{\omega}_-$
$\hat{k}\beta_b$
$\hat{\omega}_-$
$\hat{\omega}_+$
$\hat{\omega}$
$-\hat{\omega}_2$
$-\hat{k}$
$\hat{k}$
$\hat{\omega}_2$

Fig. 7(a)

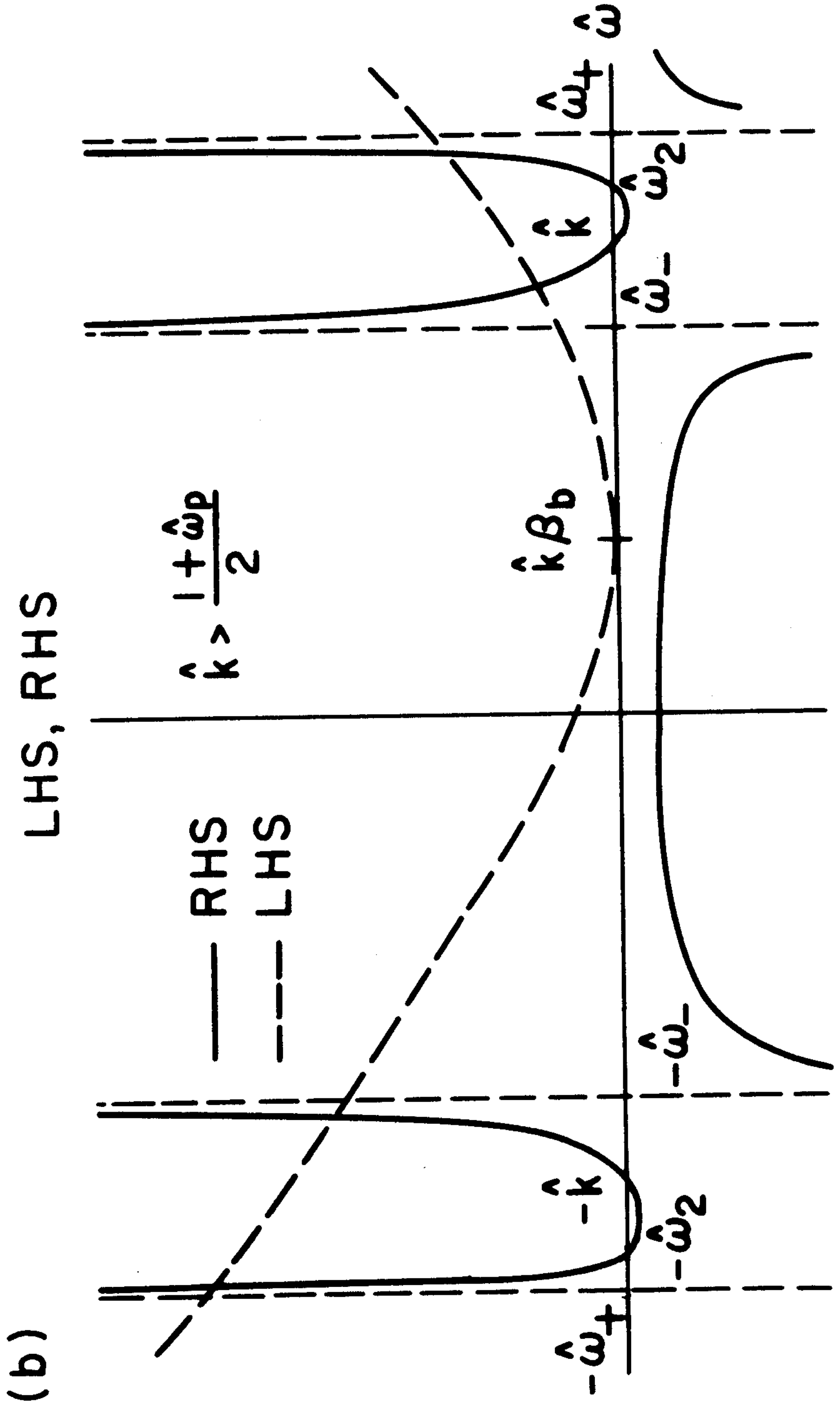
(b)
LHS, RHS
RHS
LHS
$\hat{k} > \frac{1+\hat{\omega}_p}{2}$
$\hat{\omega}$
$\hat{\omega}_+$
$\hat{\omega}_2$
$\hat{k}$
$\hat{\omega}_-$
$\hat{k}\beta_b$
$-\hat{\omega}_-$
$-\hat{k}$
$-\hat{\omega}_2$
$-\hat{\omega}_+$

Fig. 7(b)

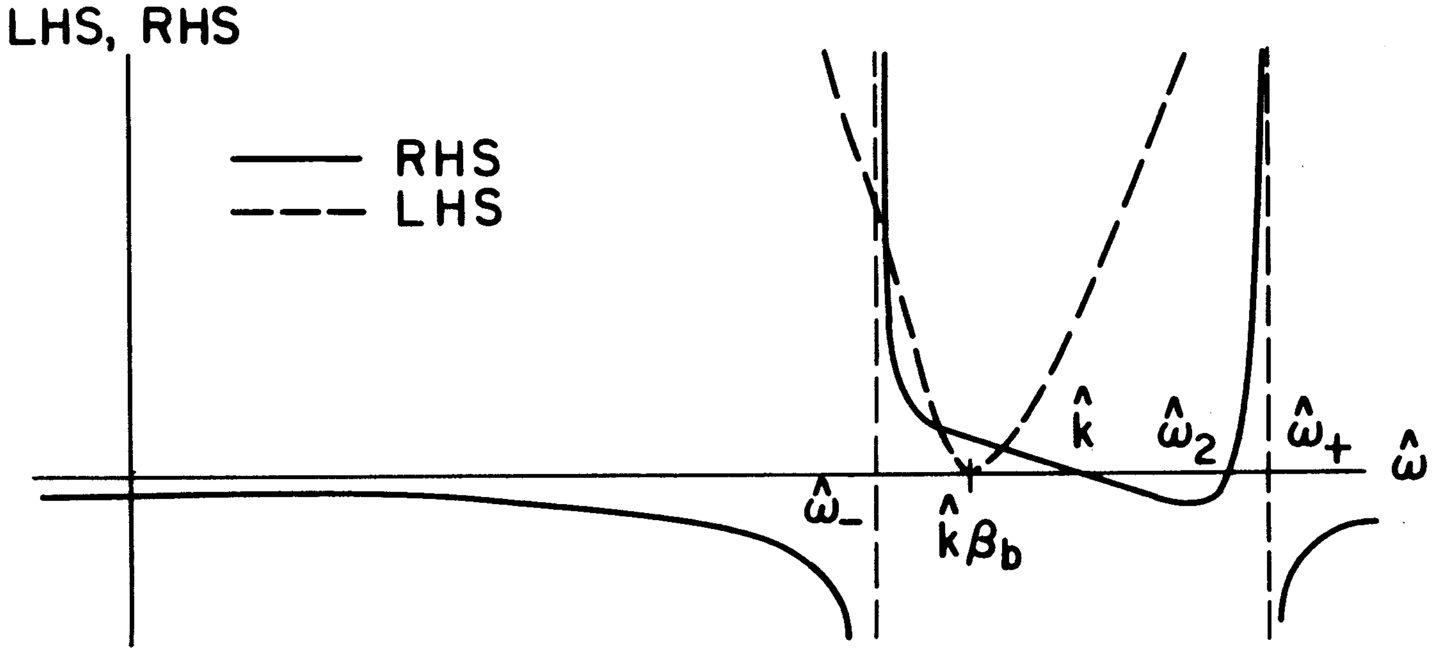
LHS, RHS
RHS
LHS
$\hat{\omega}_-$
$\hat{k}\beta_b$
$\hat{k}$
$\hat{\omega}_2$
$\hat{\omega}_+$
$\hat{\omega}$

Fig. 8

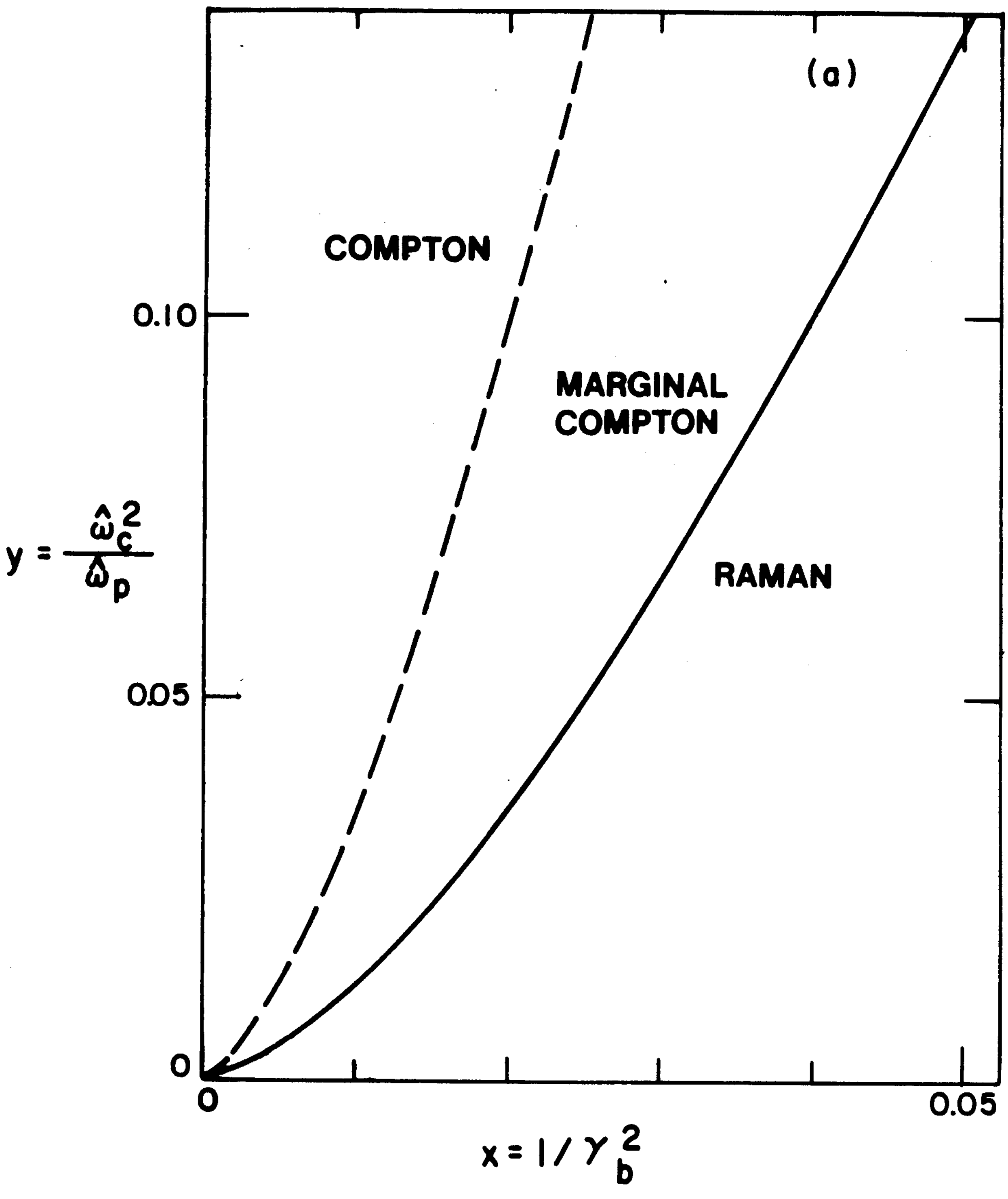
(a)
COMPTON
MARGINAL COMPTON
RAMAN
0.10
0.05
0
$y = \frac{\hat{\omega}_c^2}{\hat{\omega}_p}$
0
0.05
$x = 1/\gamma_b^2$

Fig. 9(a)

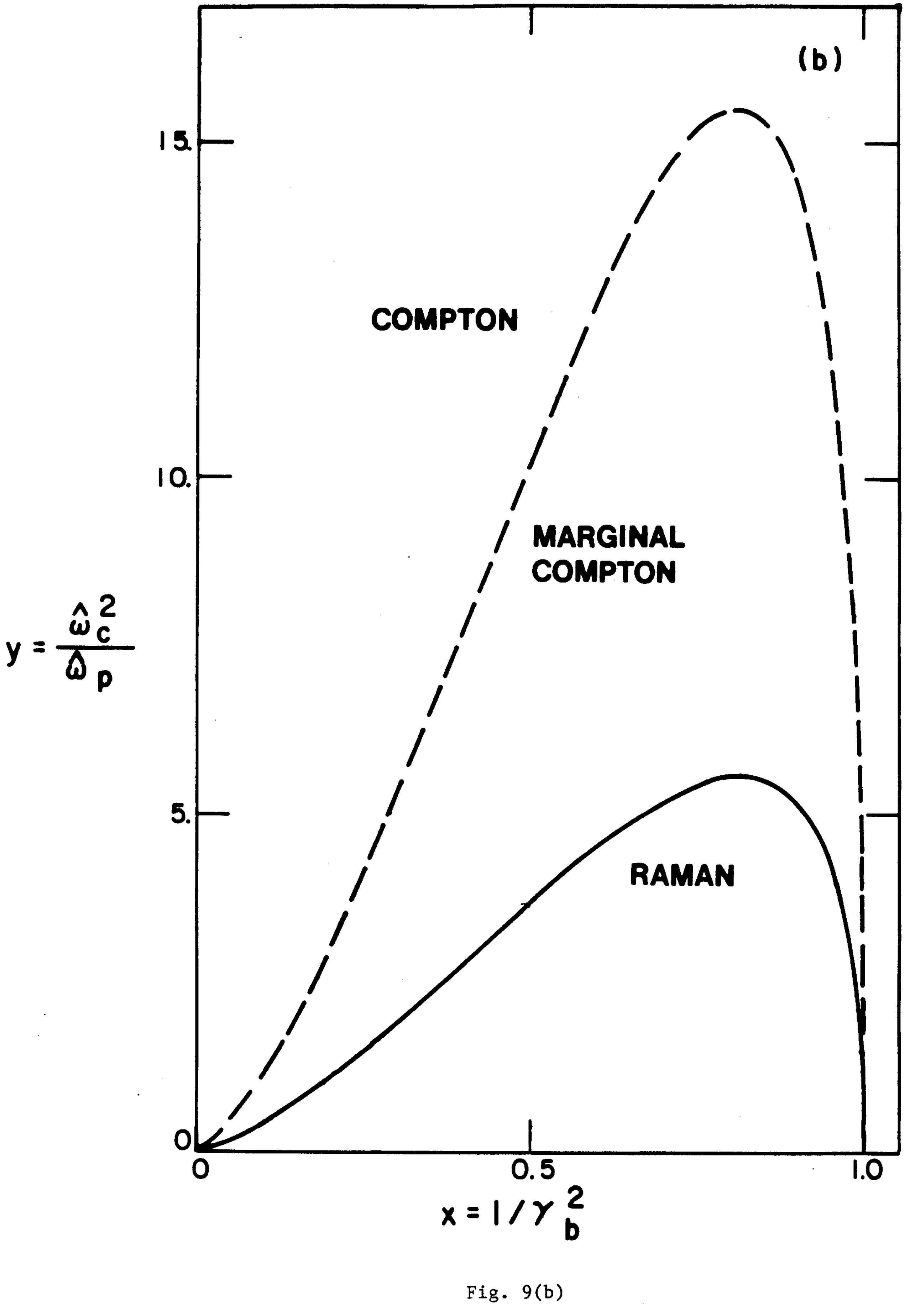
(b)
15.
10.
5.
0
0
0.5
1.0
COMPTON
MARGINAL
COMPTON
RAMAN
$y = \frac{\hat{\omega}_c^2}{\hat{\omega}_p}$
$x = 1/\gamma_b^2$

Fig. 9(b)

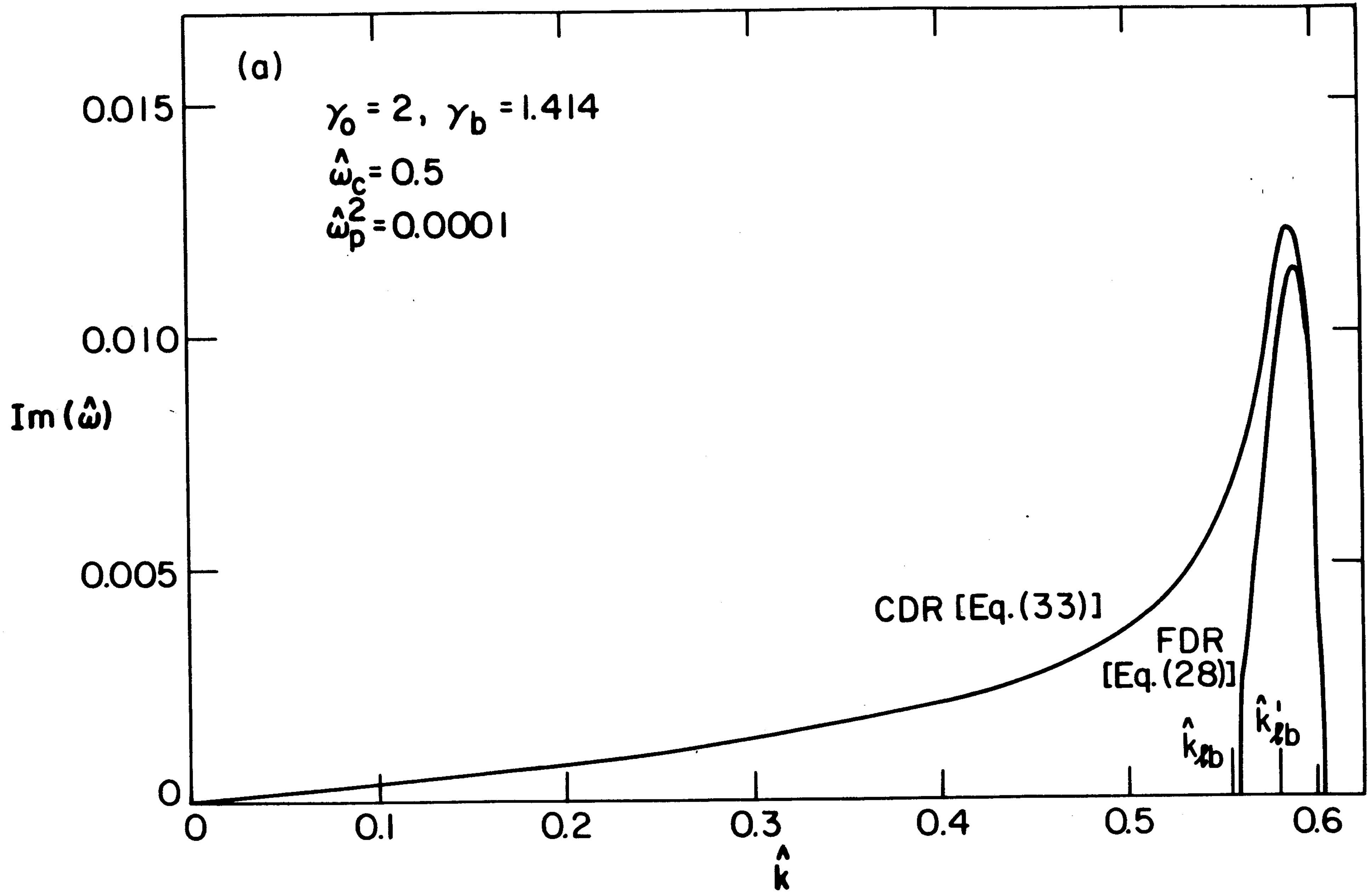
(a)
$\gamma_o = 2,\ \gamma_b = 1.414$
$\hat{\omega}_c = 0.5$
$\hat{\omega}_p^2 = 0.0001$
0.015
0.010
0.005
0
$\mathrm{Im}(\hat{\omega})$
CDR [Eq.(33)]
FDR
[Eq.(28)]
$\hat{k}_{\ell b}$
$\hat{k}'_{\ell b}$
0
0.1
0.2
0.3
0.4
0.5
0.6
$\hat{k}$

Fig. 10(a)

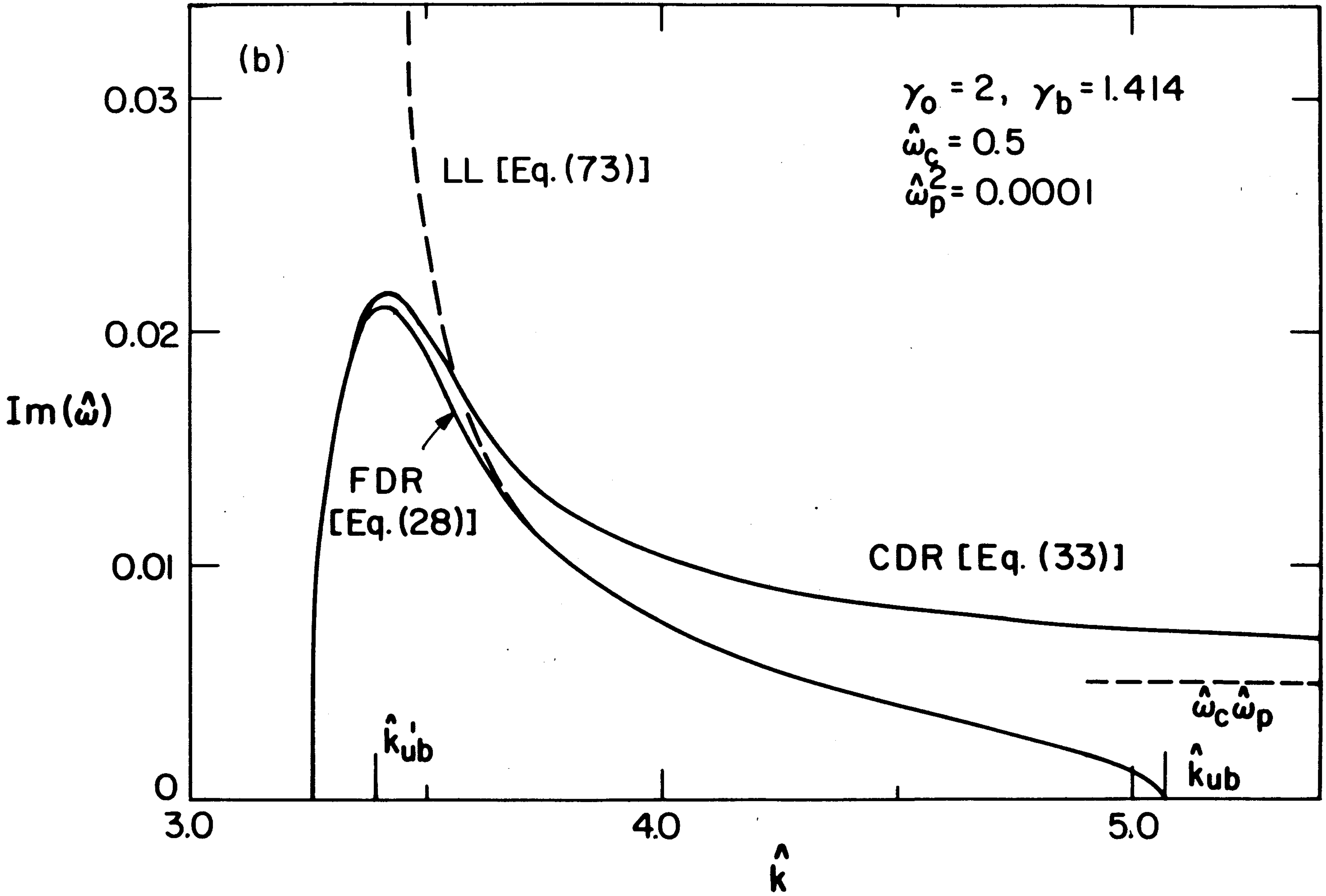
(b)
$\gamma_o = 2, \ \gamma_b = 1.414$
$\hat{\omega}_c = 0.5$
$\hat{\omega}_p^2 = 0.0001$
LL [Eq. (73)]
FDR [Eq. (28)]
CDR [Eq. (33)]
$\hat{\omega}_c \hat{\omega}_p$
$\hat{k}'_{ub}$
$\hat{k}_{ub}$
$\mathrm{Im}(\hat{\omega})$
0.03
0.02
0.01
0
3.0
4.0
5.0
$\hat{k}$

Fig. 10(b)

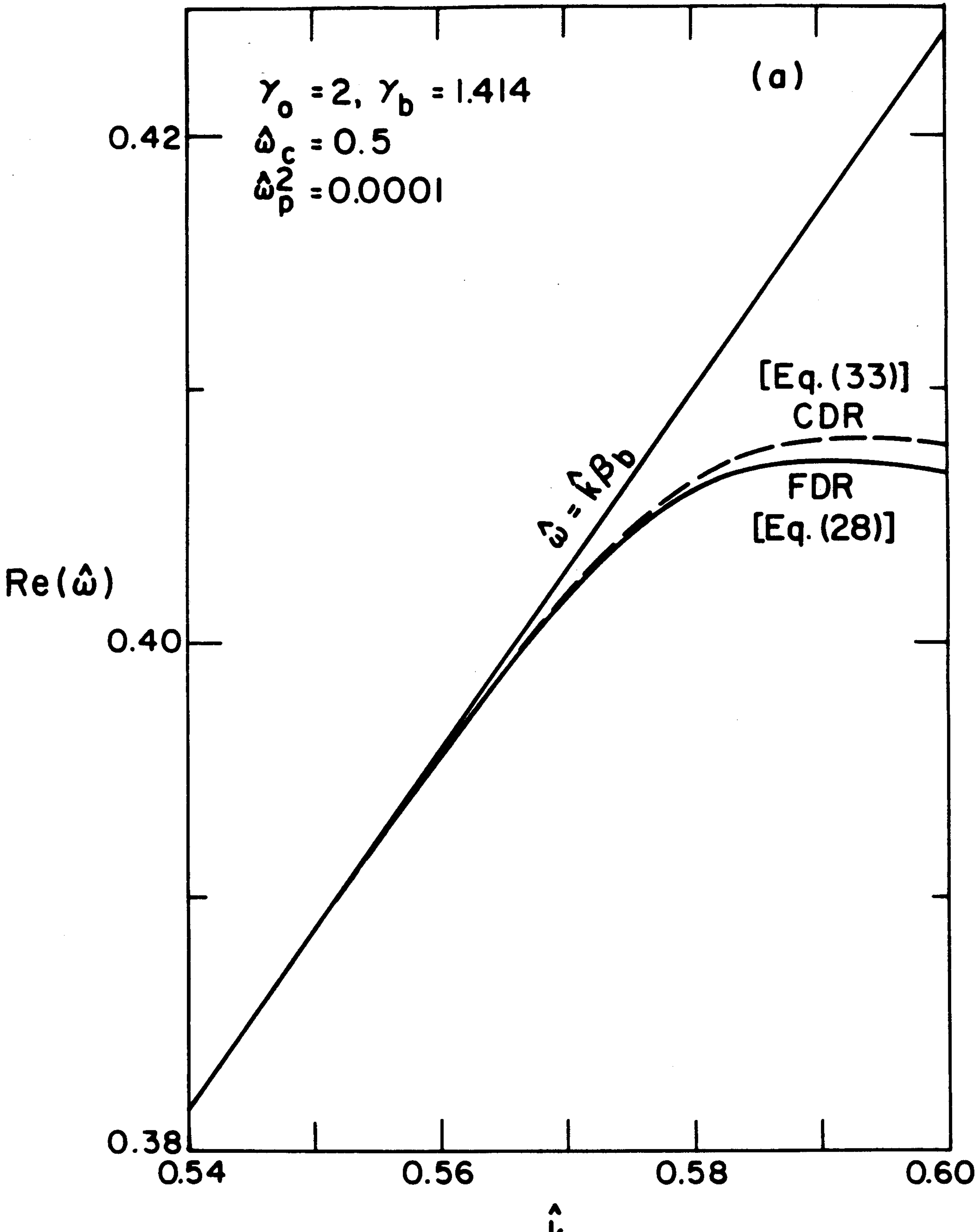

(a)
$\gamma_o = 2$, $\gamma_b = 1.414$
$\hat{\omega}_c = 0.5$
$\hat{\omega}_p^2 = 0.0001$
$\hat{\omega} = \hat{k}\beta_b$
[Eq. (33)]
CDR
FDR
[Eq. (28)]
Re($\hat{\omega}$)
0.42
0.40
0.38
0.54
0.56
0.58
0.60
$\hat{k}$

Fig. 11(a)

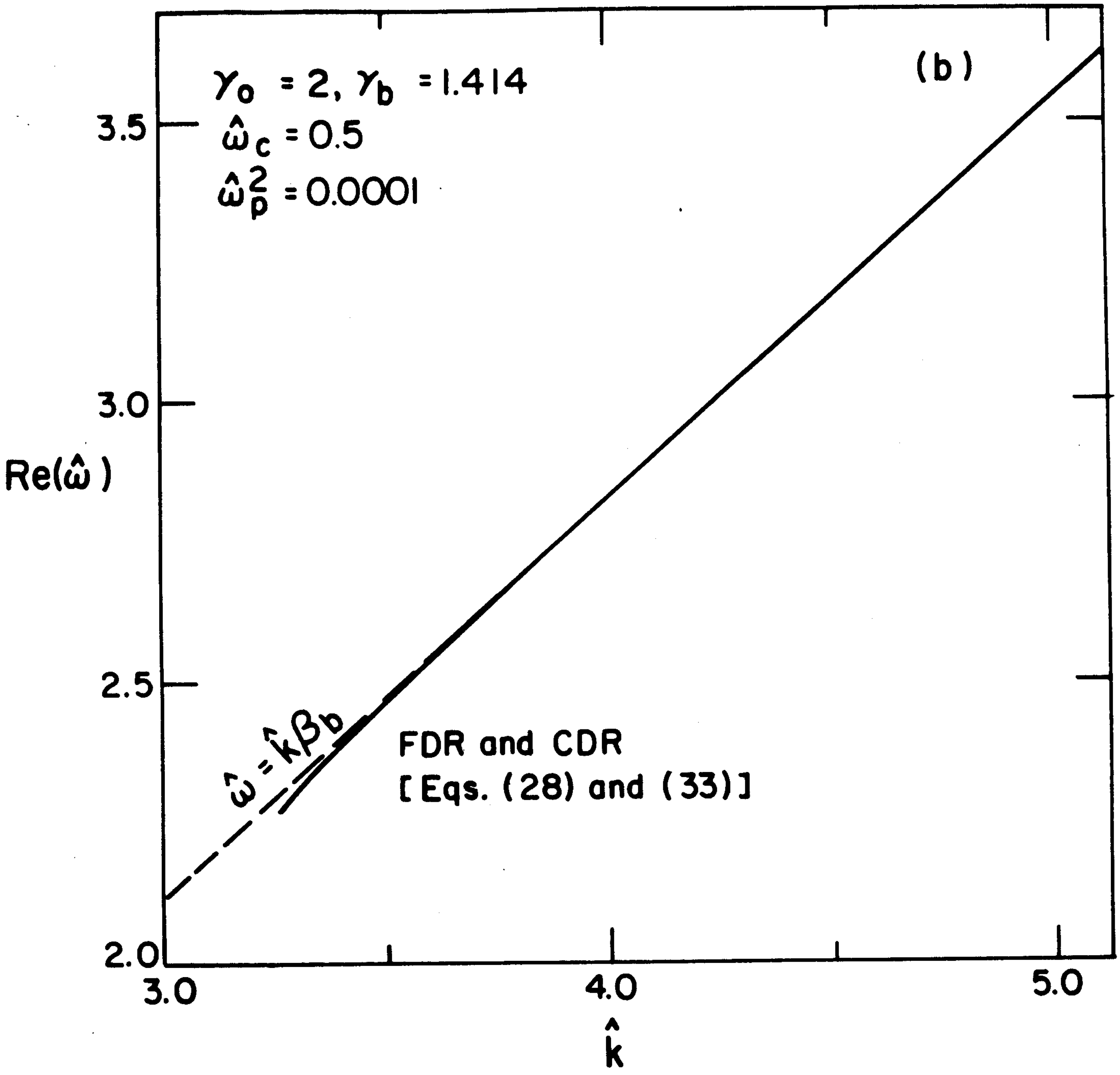
$\gamma_0 = 2$, $\gamma_b = 1.414$
$\hat{\omega}_c = 0.5$
$\hat{\omega}_p^2 = 0.0001$
(b)
3.5
3.0
2.5
2.0
Re($\hat{\omega}$)
$\hat{\omega} = \hat{k}\beta_b$
FDR and CDR
[Eqs. (28) and (33)]
3.0
4.0
5.0
$\hat{k}$

Fig. 11(b)

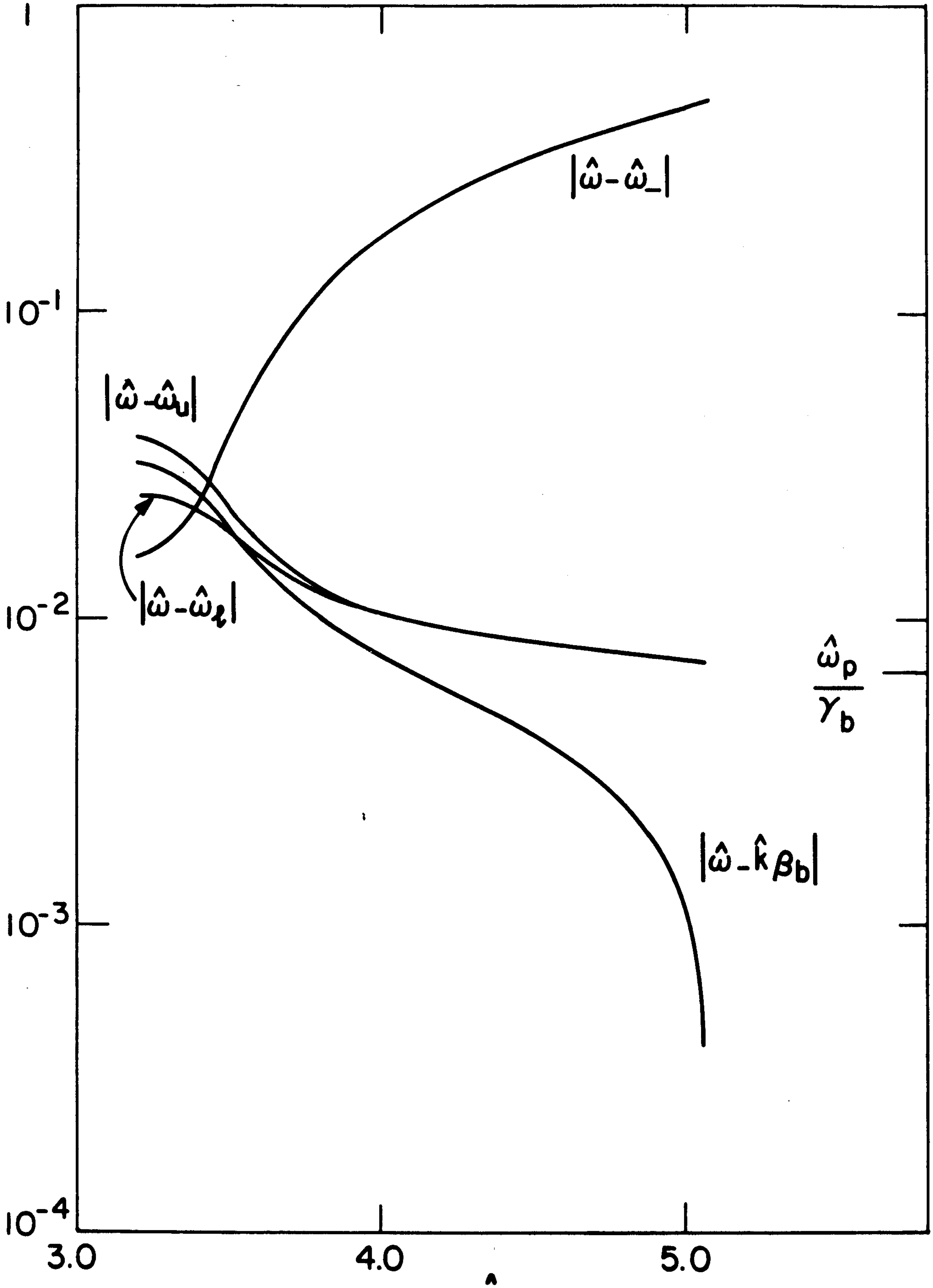
1
10^{-1}
10^{-2}
10^{-3}
10^{-4}
3.0
4.0
5.0
$\hat{k}$
$|\hat{\omega}-\hat{\omega}_-|$
$|\hat{\omega}-\hat{\omega}_u|$
$|\hat{\omega}-\hat{\omega}_\ell|$
$\frac{\hat{\omega}_p}{\gamma_b}$
$|\hat{\omega}-\hat{k}\beta_b|$

Fig. 12

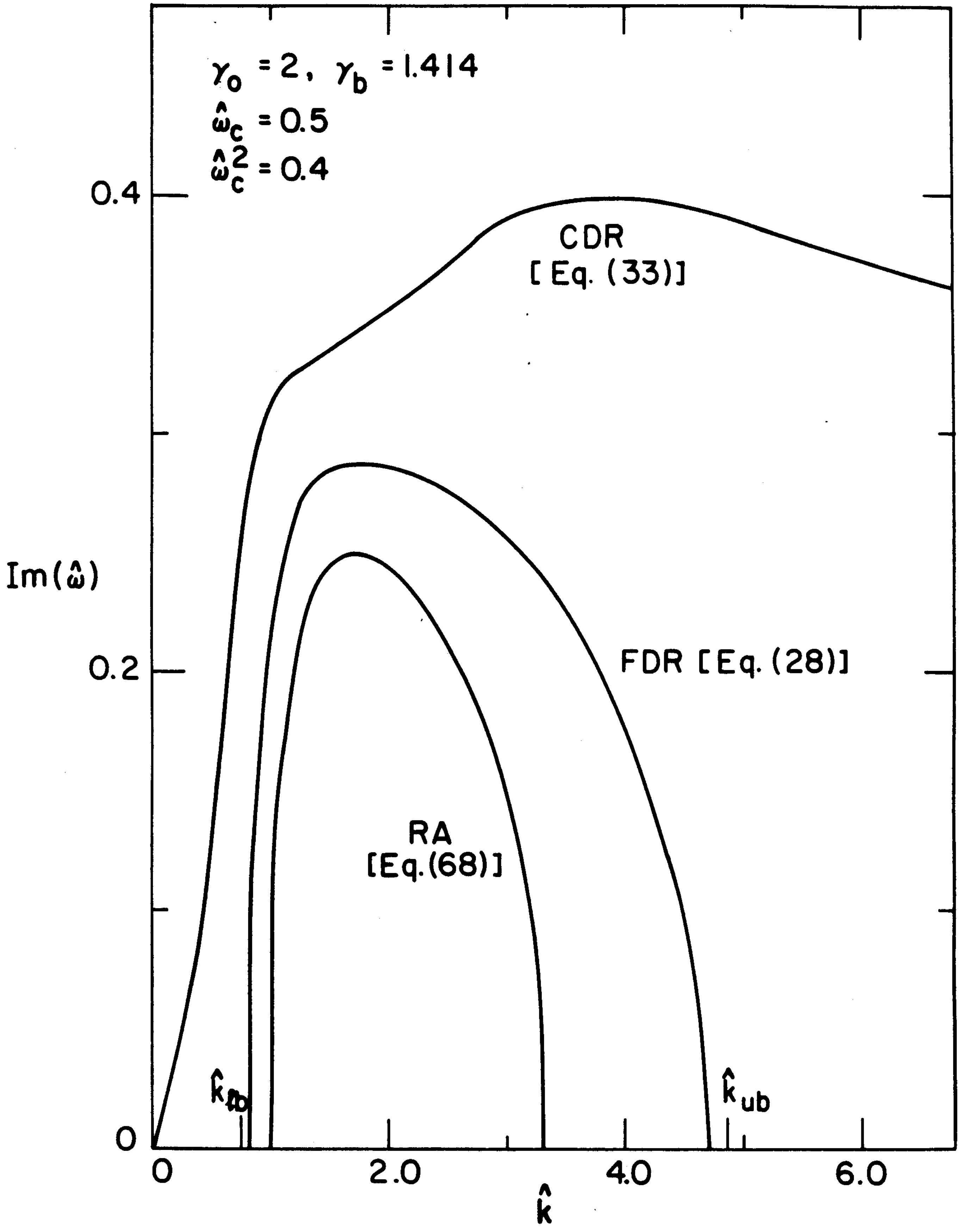
$\gamma_0 = 2,\ \gamma_b = 1.414$
$\hat{\omega}_c = 0.5$
$\hat{\omega}_c^2 = 0.4$
0.4
0.2
0
Im($\hat{\omega}$)
CDR
[Eq. (33)]
FDR [Eq. (28)]
RA
[Eq.(68)]
$\hat{k}_{\ell b}$
$\hat{k}_{ub}$
0
2.0
4.0
6.0
$\hat{k}$

Fig. 13

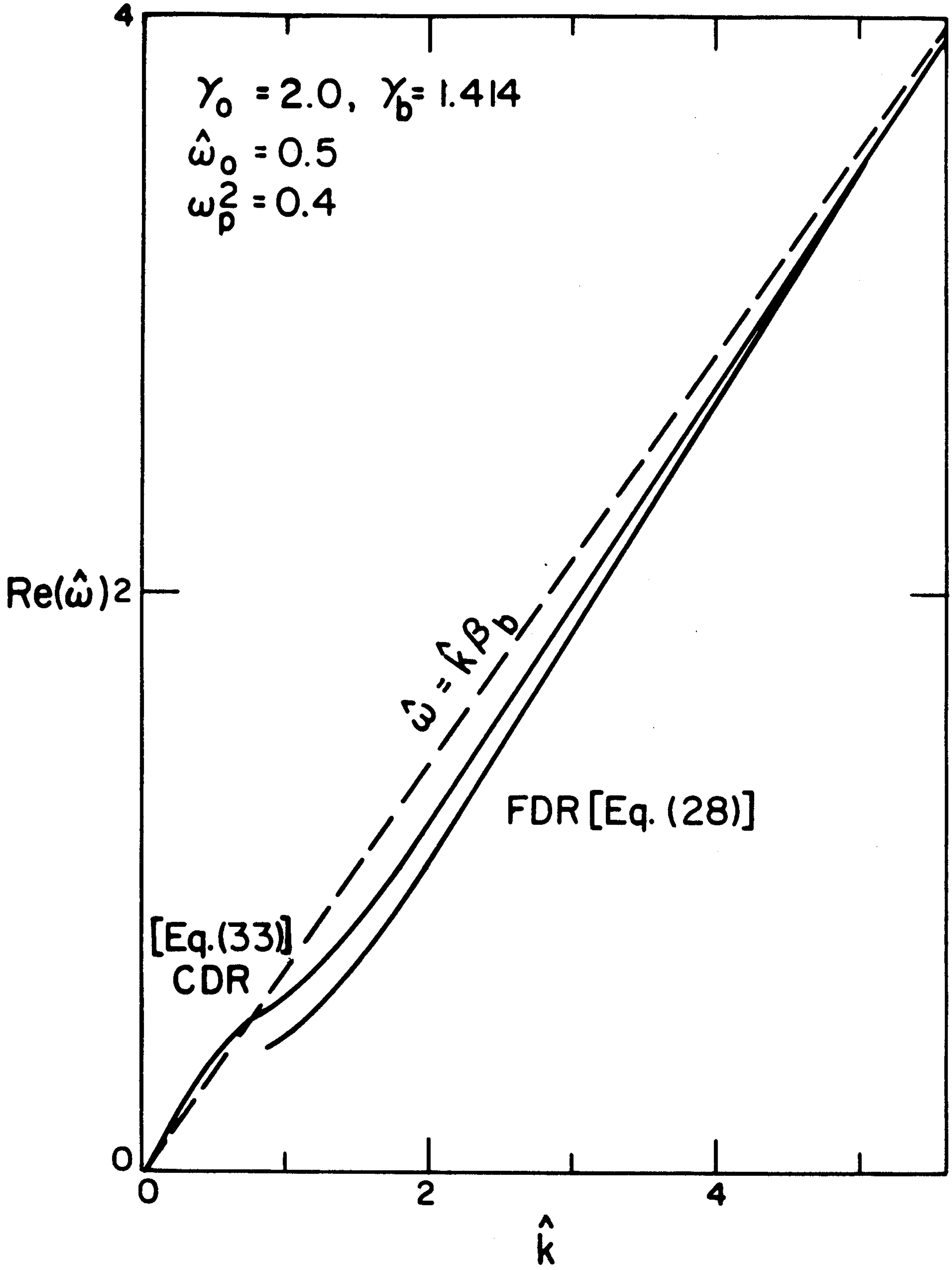
$\gamma_0 = 2.0$, $\gamma_b = 1.414$
$\hat{\omega}_0 = 0.5$
$\omega_p^2 = 0.4$
4
Re($\hat{\omega}$) 2
0
0
2
4
$\hat{k}$
$\hat{\omega} = \hat{k}\beta_b$
FDR [Eq. (28)]
[Eq.(33)]
CDR

Fig. 14

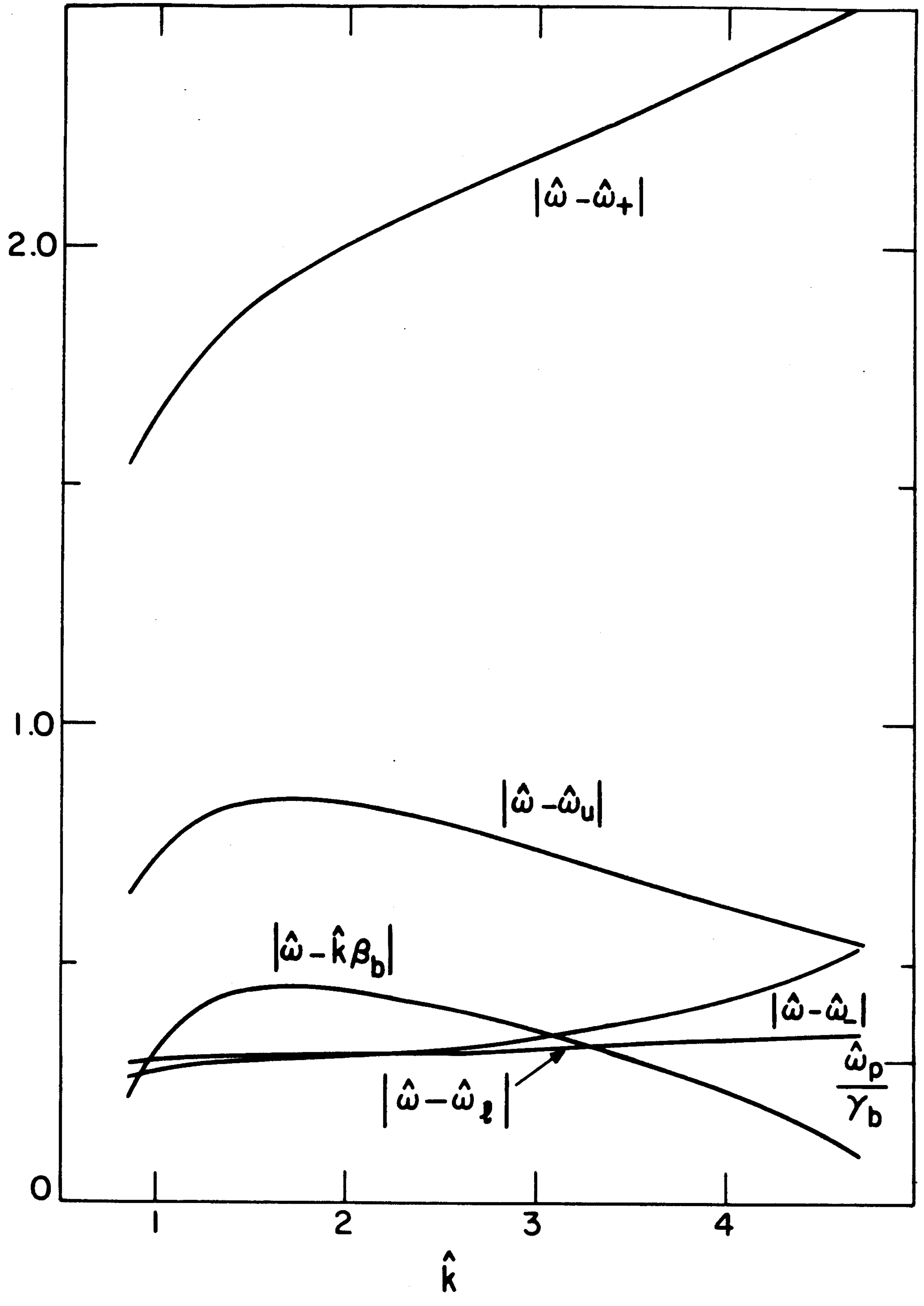
2.0
1.0
0
1
2
3
4
$\hat{k}$
$|\hat{\omega}-\hat{\omega}_+|$
$|\hat{\omega}-\hat{\omega}_u|$
$|\hat{\omega}-\hat{k}\beta_b|$
$|\hat{\omega}-\hat{\omega}_-|$
$|\hat{\omega}-\hat{\omega}_\ell|$
$\frac{\hat{\omega}_p}{\gamma_b}$

Fig. 15

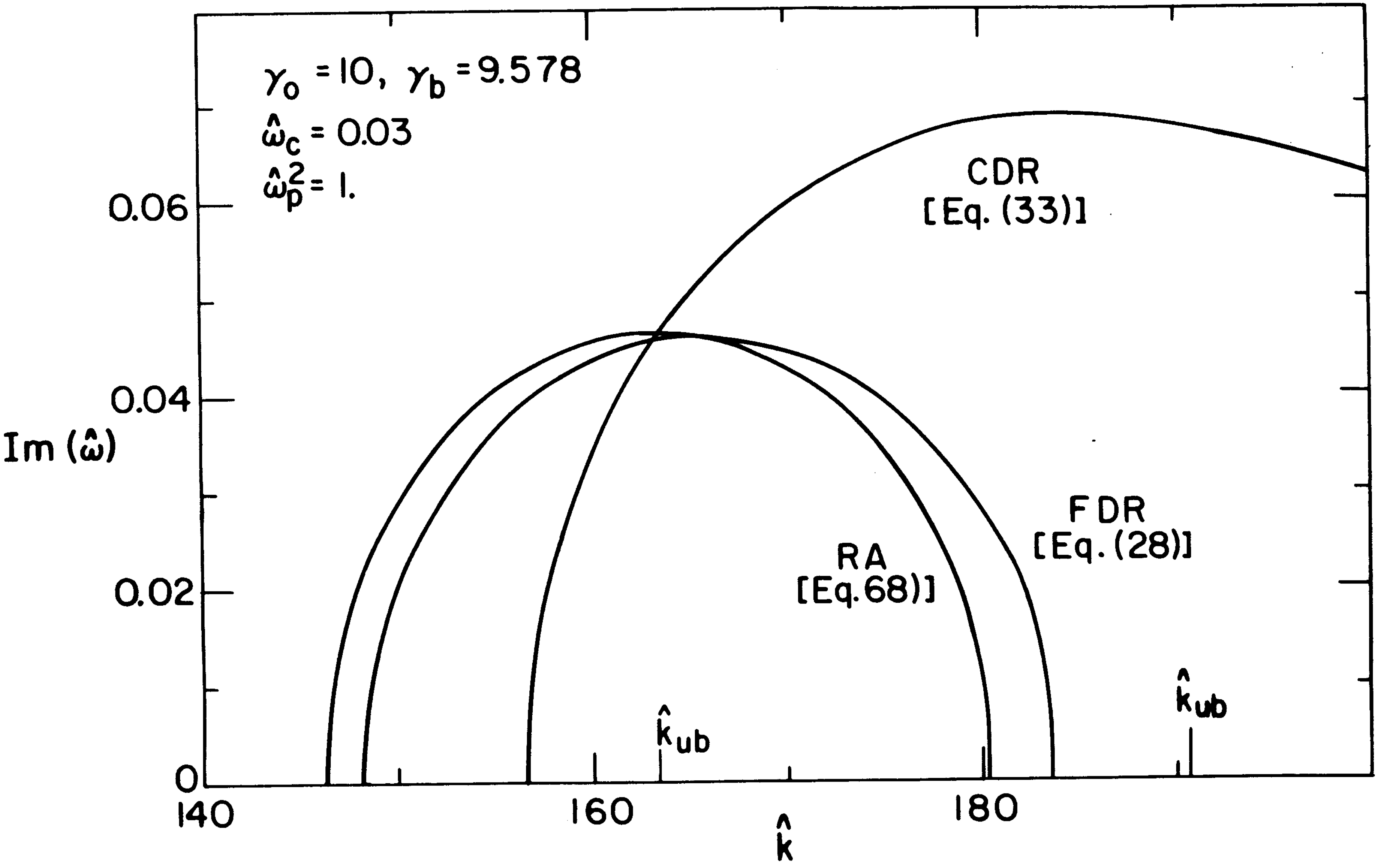
$\gamma_o = 10,\ \gamma_b = 9.578$
$\hat{\omega}_c = 0.03$
$\hat{\omega}_p^2 = 1.$
CDR
[Eq. (33)]
FDR
[Eq. (28)]
RA
[Eq.68)]
$\hat{k}_{ub}$
$\hat{k}_{ub}$
Im $(\hat{\omega})$
0.06
0.04
0.02
0
140
160
180
$\hat{k}$

Fig. 16

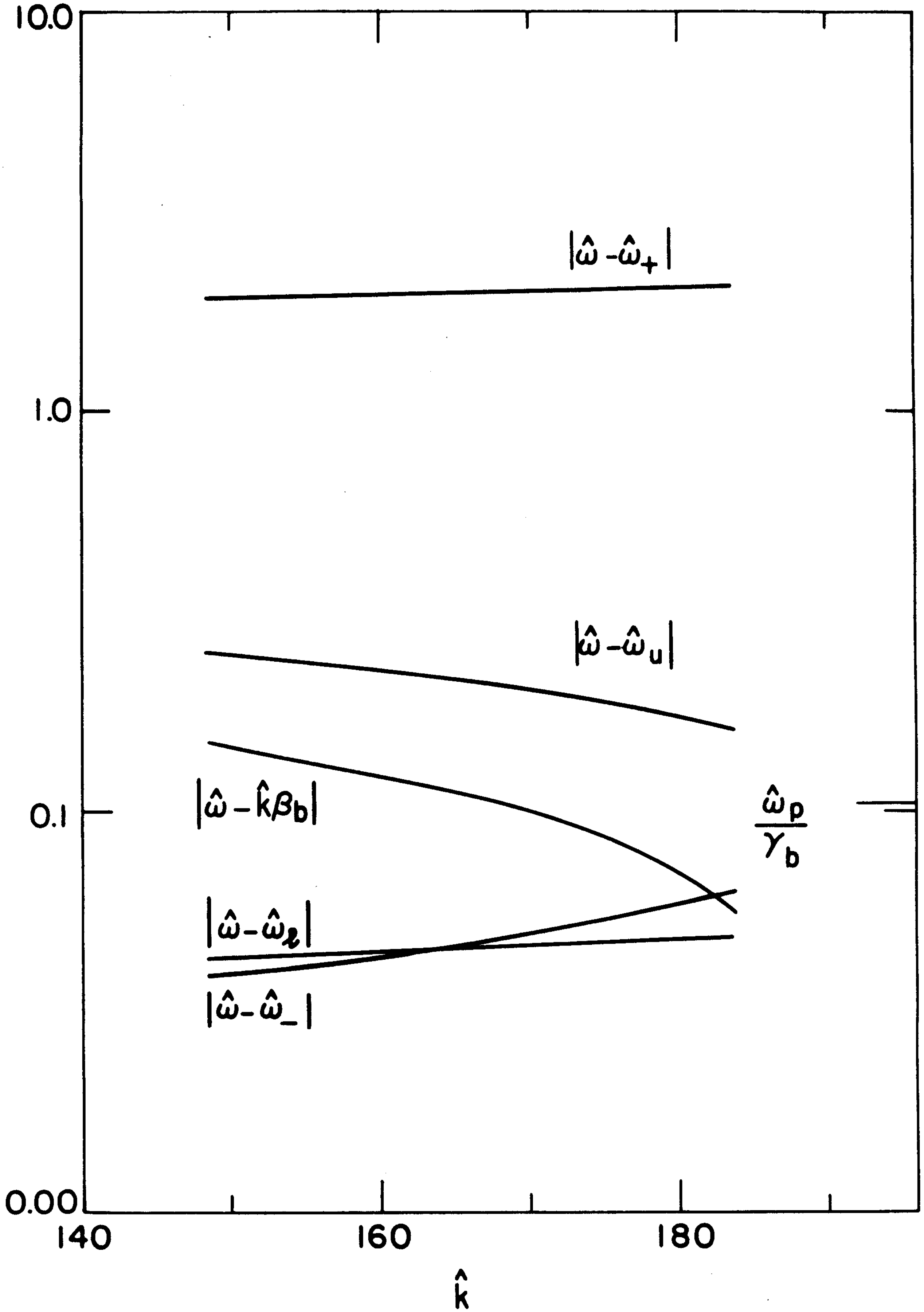
10.0
1.0
0.1
0.00
140
160
180
$\hat{k}$
$|\hat{\omega}-\hat{\omega}_+|$
$|\hat{\omega}-\hat{\omega}_u|$
$|\hat{\omega}-\hat{k}\beta_b|$
$\frac{\hat{\omega}_p}{\gamma_b}$
$|\hat{\omega}-\hat{\omega}_\ell|$
$|\hat{\omega}-\hat{\omega}_-|$

Fig. 17

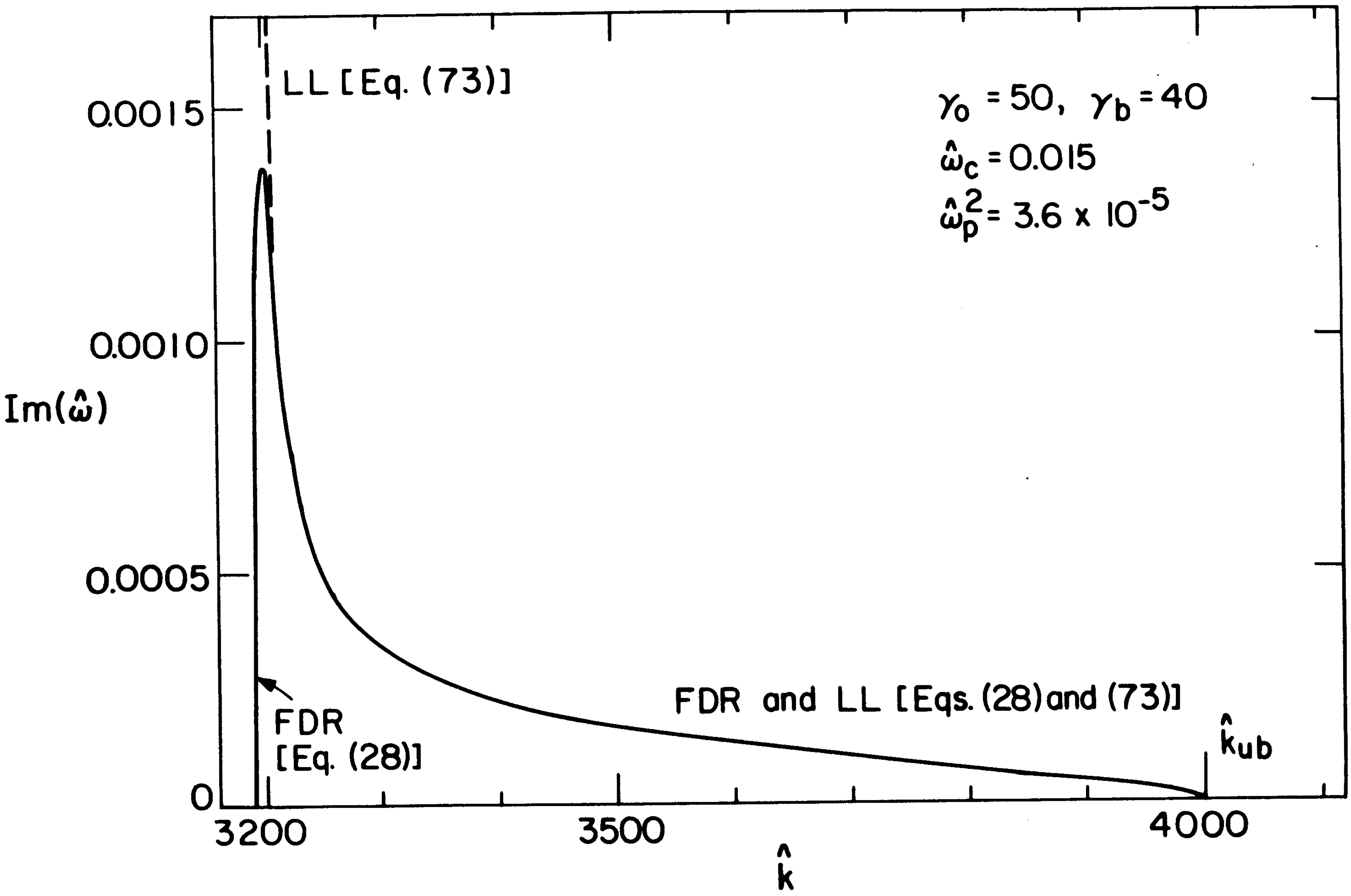
LL [Eq. (73)]
$\gamma_0 = 50, \ \gamma_b = 40$
$\hat{\omega}_c = 0.015$
$\hat{\omega}_p^2 = 3.6 \times 10^{-5}$
0.0015
0.0010
$\mathrm{Im}(\hat{\omega})$
0.0005
0
FDR [Eq. (28)]
FDR and LL [Eqs. (28) and (73)]
$\hat{k}_{ub}$
3200
3500
4000
$\hat{k}$

Fig. 18

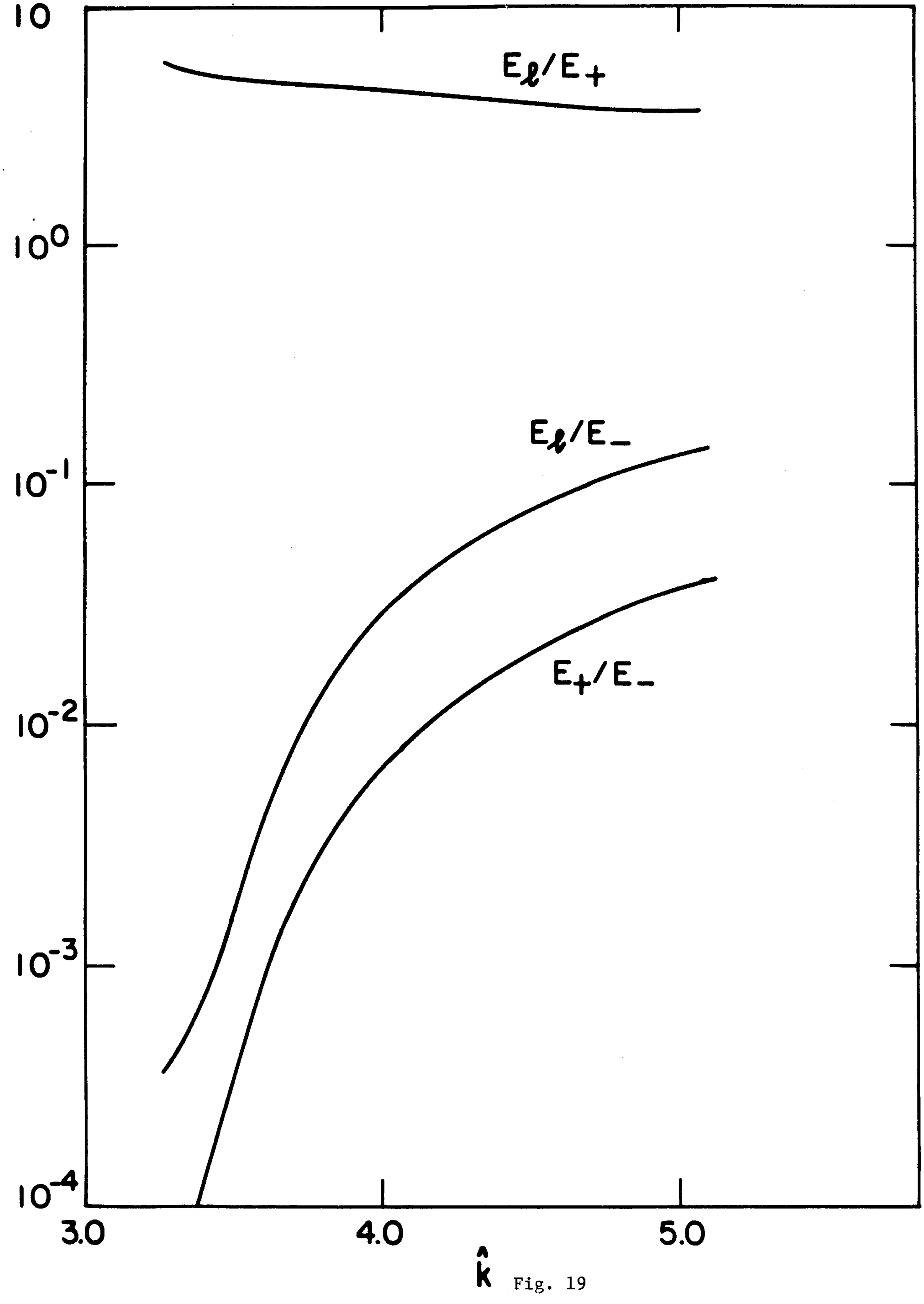

Fig. 19